

Extension and Dynamics of the Andes inferred from the 2016 Parina (Huarichancara) Earthquake

Sam Wimpenny^{1*}, Alex Copley¹, Carlos Benavente² and Enoch Aguirre²

¹COMET, Bullard Laboratories, Department of Earth Sciences, University of Cambridge, UK

²Instituto Geológico, Minero y Metalúrgico INGEMMET, Lima, Perú

*Email: *sew57@cam.ac.uk*

Accepted 23/08/2018. Received 20/08/2018; In original form 31/01/2018

1 Abstract

2 The M_w 6.1 2016 Parina earthquake led to extension of the south Peruvian Andes along a normal
3 fault with evidence of Holocene slip. We use InSAR, seismology and field mapping to determine a
4 source model for this event and show that extension at Parina is oriented NE-SW, which is parallel to
5 the shortening direction in the adjacent sub-Andean lowlands. In addition, we use earthquake source
6 models and GPS data to demonstrate that shortening within the sub-Andes is parallel to topographic
7 gradients. Both observations imply that forces resulting from spatial variations in gravitational poten-
8 tial energy are important in controlling the geometry of the deformation in the Andes. We calculate
9 the horizontal forces per unit length acting between the Andes and South America due to these po-
10 tential energy contrasts to be $4 - 8 \times 10^{12}$ N per metre along-strike of the mountain range. Normal
11 faulting at Parina implies that the Andes in south Peru have reached the maximum elevation that can
12 be supported by the forces transmitted across the adjacent foreland, which requires that the foreland
13 faults have an effective coefficient of friction $\lesssim 0.2$. Additionally, the onset of extension in parts of
14 the central Andes following orogen-wide compression in the late Miocene suggests there has been a
15 change in the force balance within the mountains. We propose that shortening on weak detachment
16 faults within the Andean foreland since $\sim 5-9$ Ma reduced the shear tractions acting along the base of
17 the upper crust in the eastern Andes, leading to extension in the highest parts of the range.

18 Key Points:

- 19 • The Parina earthquake led to NE-SW extension in the high Andes of south Peru
- 20 • Faults in the South American forelands have an effective coefficient of friction less than 0.2

- The strength of faults within the forelands modulates the stress state in the high Andes

1 Introduction

On the 1st December 2016 (22:40:26 UTC) a M_w 6.1 normal-faulting earthquake occurred ~ 70 km west of Lake Titicaca in the south Peruvian Andes (Fig. 1a). This event marks the first $M_w > 6$ extensional earthquake to occur within the Andes for 70 years, and provides a rare opportunity to study crustal deformation, lithosphere rheology and the forces driving deformation in this region.

Observations of crustal deformation within the high Andes are sparse, but are fundamental to testing models of orogen dynamics [e.g. England and Houseman, 1989; Liu et al., 2002; Flesch and Kreemer, 2010]. One particular area of contention is whether extension in the high Andes is parallel [e.g. Dalmayrac and Molnar, 1981] or perpendicular [e.g. Sébrier et al., 1985; Mercier et al., 1992] to shortening in the adjacent sub-Andean lowlands. Extension in the Andes parallel to shortening in the sub-Andes can be explained by the balance between the forces arising from differences in gravitational potential energy between the mountains and lowlands, and the forces acting through the foreland lithosphere [Dalmayrac and Molnar, 1981; Froidevaux and Isacks, 1984]. However, if extension in the Andes is perpendicular to sub-Andean shortening, shear tractions acting on the base of the Andean lithosphere are required to influence the stress state in the mountains [e.g. Liu et al., 2002].

Current observations of normal-faulting earthquakes in the Andes [Doser, 1987; Cabrera and Sébrier, 1998; Devlin et al., 2012; Jay et al., 2015] provide a limited constraint on the geometry of the extension, as the majority of the events are too small ($M_w < 5.5$) to break the full thickness of the seismogenic layer, so may not be representative of the dominant crustal strain [e.g. Brune, 1968; Jackson and White, 1989; Jackson and Blenkinsop, 1997; Scholz, 2002]. To supplement the sparse earthquake data, a number of studies have inferred the direction of extension throughout the Andes to be N-S based on slip vectors along minor fault planes [e.g. Sébrier et al., 1985; Mercier et al., 1992; Cladouhos et al., 1994; Schoenbohm and Strecker, 2009; Daxberger and Riller, 2015; Tibaldi and Bonali, 2018]. However slip on minor faults also represents a small component of the total crustal strain, and may not accurately record the bulk orientation of extension [Riller et al., 2017].

There also exists competing views regarding the orientation of shortening across the sub-Andean lowlands. Studies of earthquakes suggest shortening in the sub-Andes is parallel to gradients in the topography [Assumpção, 1992; Assumpção and Araujo, 1993; Lamb, 2000]. Alternatively, some studies have argued that the GPS velocity field in the sub-Andes can be explained by a combination of elastic strain accumulation on the locked Peru-Chile subduction interface and slip along a detachment fault beneath the sub-Andes. These elastic models assume motion on the detachment fault beneath the sub-

53 Andes has a slip vector parallel to relative plate motion between the Nazca plate and South America,
54 rather than parallel to gradients in topography [Bevis et al., 2001; Chlieh et al., 2011].

55 In this study we use geomorphology, seismology and interferometric synthetic aperture radar (In-
56 SAR) to determine a detailed source model of the 2016 Parina earthquake, and relate the pattern
57 of co- and post-seismic fault slip to the surface geomorphology. We then combine our source model
58 for the Parina earthquake with additional seismological source models, and existing GPS data, to
59 re-assess the pattern of crustal deformation in the high Andes, and its relationship with shortening
60 in the adjacent sub-Andean lowlands. We use the pattern of deformation to test models of the forces
61 driving deformation in the Andes, and investigate the rheology of the South American lithosphere.
62 Finally, we discuss possible causes for the onset of normal faulting in the high Andes at ~ 5 -9 Ma, and
63 suggest a general model for the support and evolution of mountain ranges based upon the strength of
64 faults in their forelands.

65 **2 1st December 2016 Parina Earthquake**

66 The M_w 6.1 Parina earthquake occurred in a region of south Peru that has experienced a number
67 of recent M_w 5-5.8 normal-faulting earthquakes [Dziewonski et al., 1981; Cabrera and Sebrier, 1998;
68 Ekström et al., 2012; Devlin et al., 2012; Jay et al., 2015] (Fig. 1a). Geomorphic evidence of recent
69 normal faulting in the epicentral region is scarce [e.g. Benavente et al., 2013], but has been documented
70 further north near Cuzco [Suarez et al., 1983; Sébrier et al., 1985; Mercier et al., 1992; Benavente et al.,
71 2013], and to the south near Arequipa [Lavenue et al., 2000]. The limited geomorphic expression of
72 normal faults in south Peru probably reflects the small amount of finite extensional strain in the high
73 mountains ($< 1\%$; Sébrier et al. [1985]).

74 **2.1 Local Geomorphology and Surface Ruptures**

75 Surface ruptures associated with the Parina earthquake were mapped within three days of the event
76 (Fig. 1b), and consist of two NW-SE trending sections with an along-strike length of ~ 12 km, a
77 maximum height of ~ 30 cm (downthrown to the SW), and maximum tensional opening of ~ 30 cm
78 (Fig. 2). The ruptures coincide with a 150 m-high escarpment that extends an additional 10 km NW
79 of Parina, and bounds a fluvial basin on its SW side (Fig. 1c). Tensional opening across the ruptures
80 was largest in areas where vertical offsets were also highest, which is a common feature of normal
81 faults that steepen in the near-surface [e.g. Jackson et al., 1982].

82 The northern section of ruptures consist of discontinuous, overlapping splays that map onto NW-
83 SE trending, metre-high scarps visible in pre-event satellite imagery (Fig. 2b). Both the tensional

84 opening and vertical offsets across the ruptures in the northern section were typically <10 cm (Fig.
 85 2d). In the southern section the ruptures have both opening and vertical components up to 30 cm
 86 (Fig. 2c), and form a semi-continuous trace that also coincides with a metre-high scarp (Fig. 2a).
 87 Dammed ponds on the downthrown (SW) side of the scarps pre-date the Parina earthquake (Fig.
 88 2a,b), and suggest there has probably been \lesssim 10-20 m of slip on the Parina Fault since the last major
 89 glacial epoch reset the landscape in the region at \sim 10-30 ka [Clapperton, 1983; Smith et al., 2005],
 90 implying a fault slip rate \lesssim 1 mm/yr.

91 2.2 Teleseismic Body Waveform Modelling

92 We determined the strike, dip, rake, centroid depth, source-time function and moment release of the
 93 Parina earthquake by modelling the event as a finite-duration rupture at a point source, and performing
 94 a joint inversion of long-period P and SH seismic waveforms recorded at teleseismic distances using
 95 the MT5 program of Zwick et al. [1994] (based on the algorithm of McCaffrey and Abers [1988]
 96 and McCaffrey et al. [1991]). The methodology behind this procedure has been described in detail
 97 elsewhere [see Molnar and Lyon-Caen, 1989; Taymaz et al., 1990], hence only a brief summary will be
 98 provided here.

99 Broadband seismograms recorded at stations within 30 - 90° of the earthquake epicentre were se-
 100 lected from the IRIS data management centre, and were filtered to reproduce the response of a long-
 101 period WWSSN instrument (15-100 s). Long-period waveforms are insensitive to small-scale hetero-
 102 geneity in the source region velocity structure [Taymaz et al., 1990], therefore we use a simple 1-D
 103 crustal velocity model with $V_p = 6.5 \text{ km s}^{-1}$, $V_s = 3.7 \text{ km s}^{-1}$ and density 2800 kg m^{-3} [Dorbath,
 104 1996; Schurr et al., 1999]. Inaccuracies in the velocity model typically lead to uncertainties in the
 105 centroid depth estimate of $\pm 4 \text{ km}$ for shallow ($<30 \text{ km}$) crustal events [Taymaz et al., 1990]. Accurate
 106 arrival times of the P and SH phases were picked from the broadband seismograms. The starting
 107 model for the inversion was taken as the best double-couple gCMT solution [Ekström et al., 2012],
 108 and the final model is constrained to have a double-couple moment tensor.

109 The minimum-misfit solution consists of a normal-fault source with a strike/dip/rake of $144/39/276$,
 110 a centroid depth of 12 km , and a seismic moment of $1.1 \times 10^{18} \text{ Nm}$ (M_w 6.0) (Fig. 3). The mapped
 111 surface ruptures trend parallel to the minimum-misfit strike estimate, and the sense of motion across
 112 them indicates the SW-dipping nodal plane is the fault plane.

113 Uncertainties in the source model were estimated by fixing each parameter of interest at values
 114 away from their best fit, and performing inversions in which all other parameters were free to vary.
 115 We estimate the strike to be constrained between 110 and 160° by the deterioration in fit between SH

116 waveforms recorded at stations DBIC, COYC and EFI outside this range (Fig. 4). Within this range
117 of possible strikes, the dip cannot be lower than 35° otherwise the stations MPOM and SJG would
118 lie near the P wave nodal plane, and the amplitude of the predicted P arrivals would be too low to
119 fit the observations. Mechanisms with dips $>55^\circ$ do not fit the observed waveforms as they predict
120 the incorrect SH first motion at stations FFC and SSPA. The rake must be in the range 250 - 300° to
121 fit the SH first motions and amplitudes at stations DBIC, COYC, EFI and MESJ (Fig. 4). All the
122 models that fit the observed waveforms have a slip vector azimuth between 211° and 245° (NE-SW).
123 Centroid depths greater than 20 km cannot match the observed SH waveforms as the direct S and
124 reflected sS phases separate, which is not observed (e.g. see clear waveform misfits at stations EFI
125 and COYC in Fig. 4). For all inversion results with a good fit to the observed waveforms, the seismic
126 moment is $0.9 - 1.4 \times 10^{18}$ Nm (M_w 5.9-6.1).

127 **2.3 Co-seismic InSAR: Observations**

128 We formed Sentinel-1 ascending- and descending-track interferograms covering the co-seismic period
129 of the Parina earthquake using the European Space Agency's SNAP software (<http://step.esa.int/main/>). The effect of topography on phase in the interferograms was removed using an SRTM
130 3-arcsecond elevation model [Farr et al., 2007], following which we phase filtered the interferograms
131 [Goldstein et al., 1988], and unwrapped using the statistical-cost network-flow algorithm (SNAPHU)
132 of Chen and Zebker [2001]. Additional information about the interferograms is provided in Table 3 in
133 the Supplementary Information.

135 The wrapped interferograms (Fig. 5) show 5-6 concentric, elongate fringes (corresponding to
136 a maximum of ~ 15 cm of line-of-sight displacement) oriented \sim NW-SE in both the ascending and
137 descending track, which is consistent with ground motion resulting from a fault with the same geometry
138 as our body-waveform solution. In addition, the similar pattern of displacement in the ascending and
139 descending tracks implies the majority of the deformation was vertical, which is consistent with motion
140 on a dip-slip fault [e.g. Copley et al., 2015]. The smooth fringe pattern, located to the SW of the
141 surface ruptures, and the higher fringe density in the NE than the SW of the displacement patch,
142 implies the majority of slip remained buried on a fault that dips SW, and has an up-dip projection
143 coincident with the surface ruptures. The along-strike width of the fringes is ~ 15 km, and faults that
144 are ~ 15 km long typically produce M_w 6.0-6.5 earthquakes [Wells and Coppersmith, 1994].

2.4 Co-seismic InSAR: Modelling

We determine the source parameters of the fault responsible for the 2016 Parina earthquake by inverting the InSAR measurements of surface displacement for the best fitting constant-slip, rectangular, elastic dislocation [Okada, 1985] using a simulated annealing algorithm that minimizes the root-mean-square (RMS) misfit between model and observations [e.g. Copley et al., 2015]. We solve for the location of the fault plane, its length, width, strike, dip, rake, the amount of slip and a constant offset and linear ramp in line-of-sight (LOS) across each interferogram to account for long-wavelength atmospheric and orbital artefacts. The interferograms are down-sampled uniformly over the inversion window to 200×200 m pixels to reduce the number of data points in the inversion to $\sim 70,000$. The starting model for the inversion is taken to be the SW-dipping nodal plane of our minimum-misfit body-waveform solution.

To assess the fit between the models and the observations, we estimate the noise levels in the interferograms using the magnitude of phase variations within non-deforming regions. Noise in the interferograms leads to apparent LOS variations between 1.0 and 1.1 cm in the ascending interferogram, and between 0.8 and 0.9 cm in the descending interferogram.

The inversion results suggest the InSAR data are best-fit by ~ 0.5 m of slip buried on a 13 km long normal fault with a strike/dip/rake of 135/40/250 that mostly ruptured between 3 and 10 km depth (Fig. 6). The surface projection of the best-fit fault plane is coincident with the surface ruptures. RMS residuals between the best-fit model and the InSAR observations are 0.8 cm for the ascending track and 0.9 cm for the descending track, therefore the data are fit to within the noise levels, and a more complex model of distributed fault slip is not required or justified by the data.

To test the sensitivity of the InSAR measurements to changes in the fault geometry, we performed a grid search of inversions in which each fault parameter was independently fixed at a range of values, whilst all others could vary, and measured how the misfit evolved (Fig. 7). We find that fault planes with strike = $120 - 145^\circ$, dip = $35 - 55^\circ$, rake = $250 - 270^\circ$, top depth = $1.5 - 4.5$ km and bottom depth = $6 - 14$ km can match the InSAR observations to within the noise levels. Together the range of acceptable solutions allows the slip vector azimuth to be between 230° and 280° (Fig. 7). The teleseismic waveform modelling constrains the slip vector azimuth to be between 211° and 245° , therefore the range of slip vectors consistent with all of the InSAR, seismology and surface rupture constraints have an azimuth of $230-245^\circ$ (NE-SW; see Fig. 7).

2.5 Post-seismic Deformation

Models of co-seismic fault motion indicate the majority of slip in the Parina earthquake remained buried below 3 km depth (Figs. 6, 7). However the 10-30 cm high surface ruptures measured three days after the earthquake suggest that some co-seismic slip reached the surface. Decreasing co-seismic slip on faults at shallow depths is common [e.g. Fialko et al., 2005] and has previously been observed for normal faults [e.g. Copley, 2012; Bie et al., 2014]. Limited shallow co-seismic slip is likely to reflect either inelastic deformation of the near-surface [Kaneko and Fialko, 2011], rate-strengthening frictional properties of the shallow fault zone [Marone and Scholz, 1988; Scholz, 1998], or both. In the latter case, the fault may creep post-seismically ('afterslip'), causing transient, short-wavelength surface deformation near the co-seismic rupture.

We formed interferograms covering the first 8 months following the Parina earthquake (Fig. 8a). In addition, we also generated a time-series of post-seismic deformation by extracting the relative LOS motions to either side of the surface ruptures from a series of interferograms that were formed with a common post-earthquake acquisition (collected within 19 days of the earthquake) as the reference image in each pair.

The descending-track interferograms reveal a sharp offset in the LOS displacement field across the central section of surface ruptures, with the size of the offset increasing with time after the earthquake (Fig. 8a,f). The LOS offset decays with distance perpendicular to the surface ruptures over a length scale of ~ 3 -5 km (Fig. 8f), indicating the majority of post-seismic deformation is within the top 5 km of the crust. Post-seismic signals are less clear in the ascending-track interferograms due to the larger component of atmospheric noise (Supp. Fig. 14). The temporal evolution of the post-seismic deformation follows a typical logarithmic transient decay [e.g. Smith and Wyss, 1968; Ingleby and Wright, 2017] with a relaxation time of 12 days (Fig. 8g), which is similar to estimates from a number of other studies [e.g. Savage et al., 2005; Fielding et al., 2009].

We interpret the post-seismic InSAR observations to reflect shallow afterslip on the up-dip extension of the co-seismic fault plane, and not shallow poro-elastic deformation [e.g. Peltzer et al., 1998; Fielding et al., 2009], because the sharp step in LOS directly correlates with the location of the co-seismic surface ruptures, and the polarity of the LOS motions are the same as those in the earthquake. We inverted the observed surface displacements 6 months after the Parina earthquake for the best fit, constant-slip fault (as in Section 2.4) with the rake fixed to that of the co-seismic fault model. The post-seismic InSAR measurements are consistent with ~ 6 -7 cm of afterslip on a fault with equivalent strike, dip and length to the co-seismic fault plane, but with afterslip focused between 0 and 4 km depth (Fig. 8b,d). However the constant-slip model cannot match both the smooth LOS displacement

208 pattern south of the surface ruptures, and the sharp change in LOS across the central section of the
209 ruptures (Fig. 8a,f), indicating that afterslip did not extend to the surface along the whole fault. In
210 addition, a small region of symmetrical footwall uplift and hangingwall subsidence across the southern
211 section of surface ruptures requires a locally steeper-dipping fault plane of $\sim 70^\circ$ to fit the observed
212 LOS motion in that area (Fig. 8a,f).

213 **2.6 Parina Earthquake: Summary**

214 We find that the Parina earthquake ruptured a 13 km long, NW-SE trending, SW-dipping, shallow-
215 crustal normal fault with a NE-SW ($230\text{-}245^\circ$) oriented slip vector azimuth (source models summarised
216 in Table 1). The majority of slip in the earthquake (~ 0.5 m) was buried between 3-10 km depth,
217 however a small component of slip did extend to the surface (0.1-0.3 m). Within 6 months of the
218 earthquake around 15-35% of the shallow co-seismic slip deficit was released through post-seismic
219 afterslip up-dip of the co-seismic rupture.

220 Only by combining geodetic, seismological and field observations have we been able to properly
221 quantify the uncertainty in the earthquake slip vector, and show that the direction of extension at
222 Parina is NE-SW. Seismicity surrounding Parina is typically confined to the top 10-15 km of the crust
223 (Fig. 1a), suggesting the Parina earthquake ruptured most, if not all, of the seismogenic layer. As a
224 result, the NE-SW extension is likely to be representative of the dominant strain within this region.

225 Shortening in the adjacent sub-Andean lowlands recorded in earthquake slip vectors and the orien-
226 tation of fold axes and thrust fault scarps is parallel to the direction of extension at Parina (Fig. 1a),
227 implying the mountains are locally deforming in plane strain. Smaller normal-faulting earthquakes
228 with poorly-constrained source parameters show a similar pattern, but with significant variability, in
229 which the direction of extension appears to be roughly oriented (within $\pm 45^\circ$) with shortening in the
230 adjacent sub-Andes [Cabrera and Sebrier, 1998; Devlin et al., 2012; Jay et al., 2015]. This is the
231 pattern of fault slip expected if deformation within a mountain range is controlled by a contrast in
232 gravitational potential energy between the mountains and its surrounding lowlands [e.g. Dalmayrac
233 and Molnar, 1981; Copley et al., 2009].

234 In the next section we assess the extent to which potential energy contrasts control the defor-
235 mation patterns in the Andes and the South American forelands, using well-constrained depths and
236 mechanisms of recent moderate-to-large magnitude earthquakes and existing GPS measurements.

237 **3 Dynamics of Deformation in the Andes**

238 The forces controlling deformation in mountain ranges derive predominantly from (1) relative motions
239 of the bounding plates, (2) gravity acting on density contrasts within the lithosphere, and (3) shear
240 tractions on the base of the overriding lithosphere from the underthrusting of rigid foreland material
241 [Artyushkov, 1973; England and Houseman, 1989; Wdowinski et al., 1989; Copley et al., 2011b]. These
242 forces are in a quasi-static balance with each other, viscous resistance within the ductile lithosphere,
243 and shear resistance on faults within the brittle crust. Different contributions of these forces to the
244 overall balance will be reflected in the pattern of active faulting within the mountain range and its
245 forelands [e.g. Molnar and Lyon-Caen, 1988].

246 In order to investigate the pattern of active faulting in the Andes and South America, we compiled
247 a catalogue of earthquakes with $M_w > 5$ that have been modelled using body waveforms or P wave
248 first motions from literature sources [Suarez et al., 1983; Chinn and Isacks, 1983; Kadinsky-Cade et al.,
249 1985; Doser, 1987; Assumpção and Suarez, 1988; Vega and Buforn, 1991; Assumpção, 1992; Assumpção
250 and Araujo, 1993; Tavera and Buforn, 2001; Alvarado and Beck, 2006; Emmerson, 2007; Devlin et al.,
251 2012; Scott et al., 2014] and 13 new solutions of our own (shown in Table 2). In addition, we included
252 well-constrained gCMT catalogue events with $>80\%$ double-couple moment tensors (as defined in
253 Jackson et al. [2002]) from Dziewonski et al. [1981] and Ekström et al. [2012], with hypocentral depths
254 taken from the catalogue of Engdahl et al. [1998] where available. We have included waveform-modelled
255 earthquakes with M_w 5-5.5 in this compilation, as small earthquakes provide information on the depth
256 extent of faulting in South America [e.g. Assumpção and Suarez, 1988; Assumpção, 1992; Devlin et al.,
257 2012]. Below we describe the pattern of earthquakes, in conjunction with GPS and geomorphological
258 information, and discuss the implications for the forces acting on the Andes and the South American
259 foreland.

260 **3.1 Faulting in the high Andes**

261 Moderate-magnitude earthquakes in the crust of the high Andes are infrequent, but reveal a pattern
262 of predominantly shallow (<10 - 15 km) normal and strike-slip faulting events [Doser, 1987; Cabrera
263 and Sebrier, 1998; Holtkamp et al., 2011; Devlin et al., 2012; Jay et al., 2015, This study] (Fig. 1a).
264 One exception to this pattern is seen adjacent to the Shira Uplift in south Peru, where oblique reverse
265 faulting in the high Andes was observed in the 1969 Pariahuanca earthquakes [Philip and Megard,
266 1977; Suarez et al., 1983; Sébrier et al., 1988] (see PH1969; Fig. 1a). Otherwise the majority of
267 the reverse-faulting earthquakes are confined to regions <3000 m elevation [Suarez et al., 1983]. The
268 dependence of faulting mechanism on elevation is typical of mountain ranges in which gravitational

269 potential energy contrasts are an important factor in the forces controlling deformation [Dalmayrac
270 and Molnar, 1981; Copley et al., 2009].

271 Nearly all of the moment release from recent normal-faulting seismicity in the high Andes has been
272 focused in south Peru, whilst the Altiplano and Puna plateau have remained essentially aseismic over
273 the same time period (Fig. 1a). Geomorphological evidence of recent normal faulting is also concen-
274 trated in south Peru, with a number studies identifying metre-high Holocene fault scarps bounding
275 footwall uplifts with a few hundred metres of relief (e.g., Sangararra Fault [Suarez et al., 1983]; Tam-
276 bomachay Fault [Mercier et al., 1992]; Langui-Layo Fault [Benavente et al., 2013]; Parina Fault [This
277 study]). GPS measurements in south Peru limit the cumulative NE-SW extension rate across the
278 high Andes to <5 mm/yr [Kendrick et al., 2001; Villegas-Lanza et al., 2016], which is equivalent to
279 an extensional strain rate $< 2 \times 10^{-8}$ yr $^{-1}$ over the 250 km wide plateau. In contrast, there is no
280 evidence of recent fault-controlled relief in the Bolivian Altiplano, and the shallow crust is inferred to
281 be undeforming [Lamb and Hoke, 1997; Lamb, 2000; Weiss et al., 2016]. Schoenbohm and Strecker
282 [2009] and Zhou et al. [2013] identified a number of putative normal faults within the Puna plateau,
283 however few of those mapped were associated with Holocene surface ruptures, and their estimated slip
284 rates are $\lesssim 0.1$ mm/yr over the last 0.5 Myrs. Therefore both the recent seismicity and Holocene fault
285 activity imply that the high Andes in south Peru is extending faster than the Altiplano, and possibly
286 faster than the Puna plateau.

287 Differences in strain rate within an isostatically-compensated mountain belt deforming in response
288 to variations in gravitational potential energy are related to differences in elevation [England and
289 Houseman, 1989; D’Agostino et al., 2014]. Crustal thickness estimates [Assumpção et al., 2013] and
290 small (<50 mGal) free-air gravity anomalies in the central Andean plateau both suggest that eleva-
291 tion contrasts on length-scales much larger than the elastic thickness of the Andean crust ($T_e \approx 10$
292 km; Rodríguez Tribaldos et al. [2017]) are predominantly isostatically supported. We isolated the
293 long-wavelength, isostatically-compensated component of the topography by filtering the SRTM 3-
294 arcsecond elevation model [Farr et al., 2007] using a Gaussian filter with a width of 100 km (i.e.
295 $\gg T_e$). We find that the recent normal-faulting seismicity in south Peru occurs in a region with the
296 highest smoothed modal elevation in the whole Andes at ~ 4500 m, whilst the Altiplano and Puna
297 have lower modal elevations of ~ 3800 m and ~ 4200 m, respectively (Supp. Fig. 15). Therefore
298 the distribution of recent normal-faulting earthquakes may reflect higher extensional strain rates in
299 the south Peruvian Andes compared to the surrounding mountains due to the region’s high relative
300 elevation [e.g. England and Molnar, 1997].

301 The current elevation contrasts influencing the extension rates within the Andes will decay expo-

302 nentially via flow of the lithosphere on a timescale that is dependent its viscosity. Using the unde-
303 forming Bolivian Altiplano as a reference, we can combine the current maximum extensional strain
304 rate estimate in south Peru, and the current elevation contrast between south Peru and Bolivia, to
305 compute a lower bound on the vertically-averaged Newtonian viscosity of the lithosphere ($\eta > 3 \times 10^{21}$
306 Pa s; see Appendix A). Assuming the forces acting on the Andes have remained constant in the late
307 Cenozoic, and given our lower bound on the lithosphere viscosity, elevation contrasts between south
308 Peru and the surrounding high Andes will decay with a time constant of at least ~ 3 Myrs, and are
309 unlikely to have existed much earlier than 10 Ma (see Appendix A).

310 Strike-slip faulting in the high Andes SW of Cuzco occurs where there are significant along-strike
311 changes in the geometry of the mountain belt and the amount of E-W shortening across the sub-Andes
312 [Kley and Monaldi, 1998] (Fig. 1a). In these isolated regions the Andes does not behave in a two-
313 dimensional manner, as there is a component of strain along-strike, and therefore balancing forces on
314 cross-sections perpendicular to the range front is not appropriate. In this study we focus on regions
315 where extension in the high Andes is parallel to shortening in the adjacent lowlands, so the forces
316 acting on the mountain belt can be treated in two dimensions [Dalmayrac and Molnar, 1981].

317 **3.2 Faulting in the Eastern Cordillera**

318 The Eastern Cordillera defines the area between the low relief, high elevation Andean plateau, and
319 the sub-Andean lowlands (Fig. 1a). Seismicity in this region consists mainly of moderate magnitude
320 reverse and strike-slip faulting, such as the 1998 M_w 6.6 Aiquile earthquake (Funning et al. [2005];
321 AQ1998 on Fig. 1a). The N-S trending strike-slip rupture of the Aiquile earthquake cut across
322 pre-existing fold-thrust belt structures that were active at ~ 10 Ma, which indicates the intermediate
323 principal stress has switched from being horizontal at the time in which the fold-thrust belt was active,
324 to vertical [Funning et al., 2005]. This transition in stress state can be accounted for by recent uplift
325 of the Eastern Cordillera [Gubbels et al., 1993; Lamb and Hoke, 1997], during which the forces due
326 to contrasts in gravitational potential energy between the Eastern Cordillera and lowlands increased,
327 such that they now balance the compressional forces transmitted across the sub-Andean ranges into
328 the orogen interior.

329 North of the Aiquile earthquake epicentre are the Cochabamba and Punata basins (Fig. 1a).
330 These asymmetrical half grabens are filled with post-Miocene sediments and are bounded by large
331 (~ 2 km basement relief), NE-SW to E-W striking normal faults [Renner and Velasco, 2000], which
332 are roughly perpendicular to the trend of the range front in the adjacent sub-Andes. Kenman [1993]
333 proposed the basins formed predominantly through range-parallel (NW-SE) extension. Faults with

334 a similar geometry relative to the orogen front are seen in southern Tibet [e.g. Armijo et al., 1986],
335 and have been attributed to the influence of potential energy contrasts driving radial spreading of the
336 mountains over the adjacent rigid foreland [e.g. Armijo et al., 1986; Copley et al., 2011b] - a feature
337 reflected in the earthquake slip vectors and GPS data from the Andes discussed in the next section. A
338 similar process may account for the range-perpendicular normal faults at Cochabamba and Punata.

339 **3.3 Faulting in the sub-Andes and Peru-Chile Trench**

340 Faulting on the western edge of the Andes is dominated by large-magnitude ($M_w > 7.5$) megathrust
341 earthquakes along the subduction interface between the Andean forearc and the subducting Nazca
342 plate [e.g. Pritchard et al., 2007; Sladen et al., 2010; Lin et al., 2013]. Slip in these megathrust
343 earthquakes is consistently parallel to independent estimates of the orientation of motion between the
344 Nazca plate and the South American shield [Norabuena et al., 1999; DeMets et al., 2010] (Fig. 9a).
345 Although there is evidence of recent reverse faulting within the Andean forearc [e.g. Hall et al., 2012;
346 Benavente et al., 2017], motion on these faults is small compared to slip on the megathrust.

347 Unlike slip on the megathrust, the slip vectors of earthquakes on the eastern side of the Andes vary
348 significantly along-strike of the mountain belt, with the most conspicuous changes occurring between
349 south Peru and northern Argentina. North of Cuzco a thrust-faulting earthquake in 1998 (Fig. 9a;
350 CZ1998) ruptured the shallow detachment beneath the sub-Andes with a NNE-directed slip vector,
351 which is oriented $\sim 70^\circ$ anti-clockwise to the Nazca-South America plate motion. Moving south
352 between southern Peru and northern Bolivia the earthquake slip vectors rotate clockwise from NNE
353 to NE (Fig. 9a). Around the Santa Cruz bend the slip vectors rotate rapidly clockwise by a further
354 $\sim 30\text{-}40^\circ$ to point $\sim E$ [Chinn and Isacks, 1983; Assumpção and Araujo, 1993; Devlin et al., 2012] (Fig.
355 9a). Finally, within the sub-Andes of southern Bolivia and northern Argentina the slip vectors remain
356 pointing $\sim E$, which is oriented $\sim 20\text{-}30^\circ$ clockwise relative to Nazca-South America plate motion. The
357 azimuth of the GPS velocity field in the eastern Andes relative to stable South America also rotates
358 clockwise between south Peru and northern Argentina, mirroring the pattern in the earthquake slip
359 vectors [Lamb, 2000; Kendrick et al., 2001; Weiss et al., 2016] (Fig. 9b).

360 Elastic strain accumulation within the Andes from oblique subduction of the Nazca plate beneath
361 the Andean forearc has been proposed to account for the rotation in the GPS velocities in the eastern
362 Andes [Bevis and Martel, 2001; Bevis et al., 2001]. Although the elastic model of Bevis et al. [2001]
363 fits the azimuth of GPS velocities south of the Santa Cruz bend, in southern Peru and northern
364 Bolivia it consistently underpredicts the northward component of the GPS velocities and earthquake
365 slip vectors (Fig. 9b,e-f; see Table 3). These spatially coherent misfits imply the elastic models are

366 not accurately capturing the orientation of the shortening direction in the sub-Andes. In addition, the
367 assumption in Bevis et al. [2001] that shortening in the sub-Andes can be modelled as slip parallel to
368 Nazca-South America plate motion on a detachment horizon beneath the sub-Andes is not consistent
369 with the observed earthquake slip vectors (Fig. 9a).

370 Alternatively, if the eastern Andes are deforming predominantly in response to horizontal contrasts
371 in gravitational potential energy, then the direction of shortening will be parallel to topographic
372 gradients [e.g. Lamb, 2000; Copley and McKenzie, 2007; Flesch and Kreemer, 2010]. We find that
373 earthquake slip vectors in the sub-Andes are consistently parallel to gradients in the topography
374 (Fig. 9b,d; Table 3). The topographic gradients also match the general pattern of clockwise rotating
375 GPS azimuths between southern Peru and northern Argentina, the northward component of the
376 GPS velocity field near Cuzco, and the rotation of the GPS velocities around the Santa Cruz bend
377 (Fig. 9b). In addition, the azimuth of shortening inferred from the GPS and earthquake slip vectors
378 are statistically better fit by the direction of topographic gradients than an elastic model of strain
379 accumulation on the Peru-Chile subduction zone (see statistical comparison in Table 3).

380 We therefore conclude that the forces resulting from relative plate motion control the orientation
381 of slip on the subduction interface on the western side of the Andes, whilst contrasts in gravitational
382 potential energy between the mountains and forelands control the orientation of slip on faults in the
383 sub-Andean belt in the east [e.g. Assumpção and Araujo, 1993; Lamb, 2000].

384 3.4 Faulting and Flexure in the South American Forelands

385 Reverse-faulting earthquakes in regions >300 km from the Andes range front (Fig. 9a) indicate
386 the South American foreland crust is breaking in response to compressional forces acting through
387 the lithosphere [Assumpção, 1992]. However, within 300 km of the Andes range front, asymmetrical
388 sedimentary basins [McGroder et al., 2015], long-wavelength, negative free-air gravity anomalies [Lyon-
389 Caen et al., 1985], and shallow extensional faulting overlying compressional faulting at the base of the
390 crust (Fig. 10, 11a,c) imply that the forelands are bending in response to the load of the Andes [e.g.
391 Lyon-Caen et al., 1985; Watts et al., 1995].

392 Evidence for extension in the Andes foreland is limited to a single M_w 6.4 normal-faulting earth-
393 quake beneath the Llanos Basin (Fig. 9a, Table 2). Long-period waveform modelling suggests this
394 earthquake had a centroid depth of 18_{-5}^{+5} km (Fig. 10). The Moho beneath the Llanos Basin is at ~ 40 -
395 45 km depth [Assumpção et al., 2013], which implies the normal-faulting earthquake reflects extension
396 in the shallow basement of the bending Andean foreland.

397 A M_w 5.3 reverse-faulting earthquake has also been recorded beneath the Llanos Basin (Fig. 11a,c,

398 Table 2). We determined the centroid depth of this earthquake by comparing synthetic waveforms
 399 to stacked vertical-component seismograms recorded at a small-aperture array in Spitsbergen using
 400 the method of Craig et al. [2012]. The observed seismograms can be matched by a reverse-faulting
 401 earthquake at a centroid depth of 28_{-2}^{+2} km (Supp. Fig. 12). Reverse faulting has also been recorded at
 402 42 km depth beneath the Madre de Dios Basin in central Peru [Assumpção, 1992] (Fig. 11a), indicating
 403 that the bending portion of the South American lithosphere probably remains in compression from
 404 26-30 km to at least the base of the crust (Fig. 11c).

405 Observations of shallow extensional earthquakes overlying deeper compressional earthquakes within
 406 the continental lithosphere are rare, and have only been documented previously in the forelands
 407 of Tibet [Molnar et al., 1977; Ni and Barazangi, 1984; Maggi et al., 2000b], and possibly in small
 408 ($M_w < 4.5$) earthquakes recorded in the forelands of the Alborz mountains [Nemati et al., 2013]. The
 409 pattern of earthquakes in both the Tibetan and Andean forelands implies that flexural stresses are
 410 large enough to break faults in underthrusting continental lithosphere.

411 If we treat the flexed South American forelands as a thin bending plate, the magnitude of the
 412 flexural stresses can be related to the curvature of the plate, and a factor that is governed by the
 413 assumed rheology of the plate [Turcotte and Schubert, 2002]:

$$\sigma_f = \frac{ET}{2(1-\nu^2)} \frac{d^2w}{dx^2}, \quad (1)$$

414 where σ_f is the maximum flexural stress, E is Young's modulus, ν is Poisson's ratio, T is either the
 415 effective elastic thickness of the plate (in a purely elastic model), or the thickness of the aseismic
 416 elastic core (in an elastic-plastic model with a constant yield stress), and $\frac{d^2w}{dx^2}$ is the curvature of the
 417 plate.

418 To estimate the curvature and effective elastic thickness (T_e) of the South American foreland
 419 beneath the Llanos Basin we followed the method of McKenzie and Fairhead [1997] and modelled
 420 the free-air gravity anomalies produced by flexure of an elastic plate overlying an inviscid mantle
 421 half-space, with the plate overlain by low-density sediments. We find the gravity anomalies in the
 422 Llanos Basin can be fit by a plate model with a T_e of at least 20 km (Fig. 11b,d). However the misfit
 423 between the modelled and observed gravity field at large T_e values increases by only a fraction of the
 424 minimum misfit, suggesting our estimate represents only a lower bound (Fig. 11d). Our results are
 425 consistent with those of Pérez-Gussinyé et al. [2007] and McKenzie et al. [2014], who find that T_e in
 426 the Andean forelands is between 15 and 25 km, which is significantly smaller than the seismogenic
 427 thickness (40-45 km; Assumpção and Suarez [1988]; Emmerson [2007]). Stewart and Watts [1997]
 428 found a larger T_e of 50 km in the Llanos Basin, however their study relied on modelling individual

429 Bouguer gravity profiles, and fixed the location of the plate break, which has typically been shown to
 430 overestimate T_e (see discussion in Jackson et al. [2008]).

431 The maximum curvature of the plate in the best-fit model is $\sim 4 \times 10^{-7} \text{ m}^{-1}$ (Fig. 11b). Assuming
 432 the plate has a Young's modulus of 10^{11} Pa and Poisson's ratio of 0.25, Eq. 1 would give a maximum
 433 extensional flexural stress of $\sim 530 \text{ MPa}$. This stress will subject normal faults in the top half of the
 434 bending plate, which dip at $\sim 35^\circ$ relative to the plate surface (e.g. Llanos Basin earthquake; Fig. 10),
 435 to average shear stresses $\lesssim 130 \text{ MPa}$. For a simple elastic-plastic plate with a constant yield stress
 436 [Turcotte and Schubert, 2002], and an elastic core $< 17 \text{ km}$ thick (based on the depth distribution of
 437 earthquakes; Fig. 11c), the maximum flexural stresses are reduced to $\lesssim 360 \text{ MPa}$, and the average
 438 shear stresses on faults to $\lesssim 90 \text{ MPa}$. Further earthquakes could reduce our estimate of the elastic core
 439 thickness, and therefore reduce our stress estimates.

440 In contrast to the bending portion of the South American forelands, the normal faulting in the
 441 high Andes and reverse faulting throughout the foreland crust $> 300 \text{ km}$ from the Andes range front
 442 appears to be primarily controlled by the forces per unit length exerted between the mountains and
 443 South America due to lateral contrasts in gravitational potential energy. In the next section we present
 444 calculations to estimate the forces acting through the South American forelands, and place an upper
 445 bound on the frictional strength of faults within the foreland crust.

446 4 Strength of the South American Forelands

447 4.1 Forces acting between the Andes and the South American Forelands

448 The forces per unit length due to potential energy contrasts between a mountain belt and its adjacent
 449 foreland can be calculated from lateral contrasts in the density structure between the two regions [e.g.
 450 Artyushkov, 1973; Dalmayrac and Molnar, 1981]. We build on the original calculations of Dalmayrac
 451 and Molnar [1981] by using new estimates of the temperature structure, chemical composition and
 452 thickness of the crust and mantle lithosphere to refine the estimates of the forces per unit length acting
 453 between the Andes and South America, following a method similar to that of Copley and Woodcock
 454 [2016]. A summary of the parameters used in the calculations is provided in Table 4, the choice of
 455 parameters and the methodology behind the calculations are described in detail in the Supplementary
 456 Information, and an overview of the calculations is provided below.

457 We compute the horizontal force per unit length exerted between the Andes and South America by
 458 integrating the differences in vertical normal stress between the mountains and forelands ($\Delta\sigma_{zz}$) from
 459 the surface to the depth of isostatic compensation ($F_{GPE} = \int \Delta\sigma_{zz} dz$) [Dalmayrac and Molnar, 1981].

460 By varying the temperature structure, composition and thickness of the crust and mantle lithosphere
 461 we find that the horizontal force per unit length acting between the Andes and the South American
 462 foreland is $\sim 4 - 8 \times 10^{12}$ N per metre along-strike of the mountain range (Fig. 12a). This result is
 463 consistent with previous studies [Dalmayrac and Molnar, 1981; Froidevaux and Isacks, 1984; Molnar
 464 and Lyon-Caen, 1988; Meijer et al., 1997; Husson and Ricard, 2004; Oncken et al., 2012], but includes
 465 a larger range of uncertainty that is related to the range in possible lithospheric mantle thickness
 466 and the poorly-constrained temperature structure beneath the Andes that had previously not been
 467 considered (e.g. Molnar and Stock [2009]; see Supplementary Information).

468 4.2 Fault Friction in the South American Forelands

469 The forces per unit length due to contrasts in gravitational potential energy acting between the Andes
 470 and South America must be balanced by the forces acting through the South American foreland
 471 lithosphere. Reverse-faulting earthquakes throughout the non-bending regions of the South American
 472 forelands, outboard of the region of normal faulting in the high Andes, implies that these forces are
 473 large enough to exceed the static frictional strength of faults in the forelands (as is also seen in the
 474 Tibetan foreland in India [Copley et al., 2011a]).

475 We construct one-dimensional yield stress profiles that reflect the stress state as a function of
 476 depth to the east of the sub-Andean belt in the bending and non-bending part of the South American
 477 foreland, and integrate the yield stress to estimate the force the lithosphere can support in these
 478 different regions ($F_{fl} = \int \Delta\sigma_{xx} dz$) [e.g. Goetze and Evans, 1979; Brace and Kohlstedt, 1980]. We
 479 then compare these estimates of foreland strength (F_{fl}) with our estimate of the forces per unit length
 480 acting through the foreland lithosphere (F_{GPE}) to place an upper bound on the frictional strength of
 481 faults in the South American crust.

482 Faults modulate the strength of the brittle portion of the lithosphere, which can be expressed as
 483 a function of the effective coefficient of friction [Turcotte and Schubert, 2002]:

$$\Delta\sigma_{xx} = \frac{2\mu'\rho gz}{\pm \sin 2\theta - \mu'(1 + \cos 2\theta)}, \quad (2)$$

484 where μ' is the effective coefficient of friction, ρ is the average crustal density, g is the acceleration
 485 due to gravity, z is the depth, θ is the angle of the fault from the vertical, and $\Delta\sigma_{xx}$ is the horizontal
 486 differential stress the faults can support. The $\pm \sin 2\theta$ term is negative if the faults are extensional
 487 and positive if they are compressional.

488 Within 300 km of the Andes range front the top $\sim 5-8$ km of the crust consists of sedimentary
 489 basins that contain no earthquakes [McGroder et al., 2015] (Fig. 11c), and that we assume support

negligible force. Outside of the sedimentary basins, earthquakes occur throughout the thickness of the crust [Assumpção and Suarez, 1988; Assumpção, 1992, This study] (Fig. 11c), and therefore we assume that stresses in the basement crust are supported by frictional resistance on faults given by Eq. 2.

Earthquakes are absent from the foreland mantle lithosphere beneath South America (Fig. 11c). A similar pattern of seismicity has been observed in other continental shield regions (e.g., India [Maggi et al., 2000a; Craig et al., 2012]; Africa [Craig et al., 2011]; Siberia [Sloan et al., 2011]), and has been attributed to the temperature of the continental lithospheric mantle generally exceeding ~ 600 °C [McKenzie et al., 2005; Jackson et al., 2008], above which mantle rocks deform predominantly by ductile creep mechanisms. We use a dry olivine dislocation creep law to estimate an upper bound on the ductile strength of the lithospheric mantle [Karato and Wu, 1993]:

$$\Delta\sigma_{xx} = S\dot{\epsilon}_r^{\frac{1}{n}} A^{-\frac{1}{n}} \exp\left(\frac{E + pV}{nRT}\right), \quad (3)$$

where S is the shear modulus, $\dot{\epsilon}_r$ is the reference strain rate which we calculate by imposing stress continuity at the brittle-ductile transition, A is a constant, n is the power-law exponent, E is the active energy, p is the pressure, V is the activation volume, R is the gas constant and T is the temperature (parameters given in Table 4). It has been suggested that upper mantle rocks at temperatures less than 750 °C may deform by low temperature plasticity (Peierl's creep) [e.g. Mei et al., 2010; England and Molnar, 2015], which would support smaller differential stresses for a given strain rate than dislocation creep. If so, the forces supported by faults in the lithosphere would be slightly higher than our estimates. However, we also perform calculations in which the lithospheric mantle supports no stress, providing an absolute upper bound on the possible forces acting on faults within the crust.

By performing a parameter sweep through the range of variables that control the shape of the yield stress envelope with depth (effective coefficient of friction, seismogenic thickness, fault dips, neutral fibre depth, elastic core thickness and sediment thickness; parameter range given in Table 4), we can define an envelope of the force that the lithosphere can support as a function of the effective coefficient of friction on crustal faults (Fig. 12b-d). We find that, in order to break in response to the $4 - 8 \times 10^{12}$ Nm⁻¹ that we estimate above to be acting through the forelands, faults in the bending and non-bending regions of South America must have an effective coefficient of friction $\lesssim 0.15$. If the lithospheric mantle supported no stress at all, which would resolve all the force acting through the foreland lithosphere onto faults in the crust, the maximum possible effective coefficient of friction would be 0.2 (Fig. 12d). If the faults in the South American crust were stronger, then they would not be breaking in earthquakes as a result of the forces per unit length generated by gravitational

521 potential energy contrasts between the Andes its bounding lowlands.

522 Our low estimate of the effective coefficient of friction on faults in the South American crust is
 523 consistent with studies that infer elevated pore-fluid pressures [Sibson, 2004] or foliated, phyllosilicate-
 524 rich fault gouges [Imber et al., 2008; Collettini et al., 2009] may reduce the frictional strength of active
 525 fault zones relative to laboratory estimates of bare rock friction [Byerlee, 1978]. Notably, faults in the
 526 forelands with an effective coefficient of friction $\lesssim 0.2$, that dip between $30\text{-}50^\circ$ (Fig. 10), will support
 527 depth-averaged shear stresses $\lesssim 110$ MPa, which is similar to our estimate derived from the analysis
 528 of flexure in Section 3.4.

529 Previous studies of the dynamics in South America based on a ‘thin-viscous sheet’ approximation
 530 [England and McKenzie, 1982] imply the deviatoric stresses acting to deform the lithosphere are rel-
 531 atively small ($\sigma'_{xx} \approx 10 - 30$ MPa; Dalmayrac and Molnar [1981]; Lamb [2000]; Flesch and Kreemer
 532 [2010]). Our estimates of the horizontal forces acting through the $\sim 100\text{-}150$ km thick foreland litho-
 533 sphere imply deviatoric stresses on the order of a few 10 's of megapascal, which is consistent with the
 534 aforementioned studies.

535 5 Discussion

536 5.1 Late Miocene Change in the Dynamics of the Andes

537 The Parina earthquake and the surrounding seismicity demonstrates that the high Andes in south
 538 Peru are currently undergoing extension. A M_w 6.2-6.8 normal-faulting earthquake recorded in 1946
 539 at Ancash in central Peru [Heim, 1949; Doser, 1987], and a M_w 5.4 earthquake in the Bolivian Altiplano
 540 (Fig. 9a), suggest that a wider region of the high central Andes is also currently extending.

541 Geological evidence of recent normal faulting in the high Andes is widespread, with examples of
 542 extensional structures in regions at elevations >3000 m from central and southern Peru [Dalmayrac
 543 and Molnar, 1981; Sébrier et al., 1985, 1988; Mercier et al., 1992; Veloza et al., 2012; Benavente et al.,
 544 2013; Kar et al., 2016], northern Chile [Tibaldi et al., 2009; Tibaldi and Bonali, 2018], southern and
 545 northern Bolivia [Mercier, 1981; Lavenue et al., 2000; Lamb, 2000] and northern Argentina [Cladouhos
 546 et al., 1994; Marrett et al., 1994; Lavenue et al., 2000; Schoenbohm and Strecker, 2009] (Figs. 9a,
 547 13). The timing of motion on these normal faults can be bracketed by cross-cutting relationships with
 548 the extensive volcanics erupted continually throughout the Andean orogeny. The earliest evidence
 549 of extension in the high Andes varies from $\sim 7\text{-}9$ Ma in southern Bolivia and northern Argentina
 550 [Cladouhos et al., 1994; Montero Lopez et al., 2010], to $\sim 5\text{-}7$ Ma in central and southern Peru [Mercier,
 551 1981; Cabrera et al., 1991; Giovanni et al., 2010; Benavente et al., 2013; Kar et al., 2016], and follows

552 an earlier period of widespread \sim E-W compression [Megard et al., 1984; Sébrier et al., 1985; Ellison
553 et al., 1989; Mercier et al., 1992; Elger et al., 2005; Tibaldi et al., 2009]. Within the central Bolivian
554 Altiplano folded Pliocene strata in the Corque-Corococo basin imply the shallow crust experienced
555 waning shortening between \sim 10 Ma and 3 Ma [Hoke and Lamb, 2007; Lamb, 2011], and has recently
556 been undeforming [Elger et al., 2005; Lamb, 2011] (Fig. 13). The transition in stress state within
557 parts of the high Andes of Peru and Argentina from dominantly compression to extension since the
558 late Miocene, and the slowing of shortening in the lower elevation Bolivian Altiplano, is indicative of
559 an orogen-wide change in the force balance.

560 Over the same time interval (\sim 5-16 Ma) paleoelevation proxies infer there has been 1-3 km of
561 surface uplift in the high Andes of southern Peru and Bolivia [e.g. Garzzone et al., 2006; Barke and
562 Lamb, 2006; Garzzone et al., 2008; Saylor and Horton, 2014; Kar et al., 2016; Garzzone et al., 2017].
563 In addition, structural reconstructions and proxies for rock exhumation have recorded a distinct shift
564 in the locus, rate and style of deformation on the eastern edge of the Andes. Prior to \sim 10 Ma
565 deformation in the eastern Andes consisted of slow, long-wavelength folding and bivergent reverse
566 faulting of lower Paleozoic strata and metamorphic basement focused in the Eastern Cordillera [Kley,
567 1996; Oncken et al., 2006; Espurt et al., 2008; Perez et al., 2016]. Since \sim 10 Ma shortening rates in the
568 eastern Andes have increased significantly [Oncken et al., 2006, 2012], and the locus of deformation has
569 propagated rapidly eastwards into the sub-Andean lowlands [Gubbels et al., 1993; Echavarría et al.,
570 2003; Gautheron et al., 2013; Perez et al., 2016], where Mesozoic foreland basin fill is exposed in short-
571 wavelength (\sim 5-10 km) anticlinal ridges bound by closely-spaced splay faults above shallow-dipping
572 detachments [e.g. Kley, 1996].

573 Any attempt to explain the onset of normal faulting in the high Andes \sim 5-9 Ma must also account
574 for the observations described above (summarised in Fig. 13).

575 **5.2 Possible causes of Normal Faulting in the High Andes**

576 Removal of dense lower crust and mantle lithosphere (delamination) could increase the gravitational
577 potential energy contrast between the mountains and forelands, leading to extension in the highest
578 parts of the Andes [e.g. England and Houseman, 1989; Garzzone et al., 2006]. Delamination has been
579 proposed to account for the composition, timing and volume of ignimbrite and mafic volcanism [e.g.
580 Kay and Mahlburg Kay, 1993], the Helium isotope ratios of hydrothermal fluids [Hoke and Lamb,
581 2007], and the possible rapid Miocene-recent uplift of the central Andes [e.g. Garzzone et al., 2006,
582 2008, 2017]. However the relationship between crustal thickening and uplift rates in the Bolivian
583 Altiplano [Lamb, 2011, 2016], and inconsistent seismic models that independently infer thick, thin

584 and variable thickness lithospheric mantle beneath the Andes [e.g. Whitman et al., 1992; Beck and
585 Zandt, 2002; Phillips et al., 2012; Priestley and McKenzie, 2013; Ward et al., 2016], call into question
586 whether delamination beneath the central Andes coeval with extension actually occurred.

587 Another mechanism that has been suggested to induce extension in the high Andes is dynamic
588 uplift of central Peru due to the subduction of the buoyant Nazca Ridge [Mercier et al., 1992; McNulty
589 and Farber, 2002; Margirier et al., 2017]. Our observations of normal-faulting earthquakes 400 km
590 south of the Nazca Ridge (Fig. 13), in addition to evidence of extensional faulting within elevated
591 regions across the Andes, irrespective of the nature of the underlying subducting plate (e.g. flat slab
592 segments; Gutscher et al. [2000]), indicates that the pattern of extension is probably unrelated to
593 subduction processes. Similarly, the timing and distribution of normal-faulting earthquakes appears
594 unrelated to the subduction zone earthquake cycle.

595 Changes in the horizontal forces supported by the lithosphere bounding the Andes could also cause
596 the onset of extension in the high mountains. The switch in shortening style in the eastern Andes
597 ~ 10 Ma from steeply-dipping reverse faulting to shallow-dipping, weak detachment faulting within
598 the foreland basin sediments could have reduced the shear stresses acting on the base of the overriding
599 Andean lithosphere, leading to the onset of extension in the high mountains, a reduction in shortening
600 rates in the Bolivia Altiplano, and enhanced shortening rates within the lowlands of the eastern Andes
601 [Babeyko et al., 2006; Oncken et al., 2012]. We explore this possibility further below.

602 The spatial relationship between normal faulting and foreland deformation style is suggestive of
603 a causal link. Late Miocene to recent normal faulting in the high Andes correlates along-strike with
604 regions of wide thin-skinned fold-thrust belts [Kley et al., 1999], the locations of low-angle thrust-
605 faulting earthquakes [Devlin et al., 2012], and thick Paleozoic and Mesozoic sediments in the adjacent
606 foreland basin [McGroder et al., 2015] (Supp. Fig. 17). In contrast, in regions where the active
607 foreland deformation style comprises predominantly reverse faulting emerging at the front of steep
608 topography (e.g., Shira Uplift of Peru [Kley et al., 1999]; Sierra Pampeanas of Argentina [Alvarado
609 and Beck, 2006]; Oriente of Ecuador [Kley et al., 1999]) the style of faulting in the adjacent high
610 Andes is dominantly compressional (Fig. 13). A particularly clear example is seen in the high Andes
611 adjacent the Shira Uplift in Peru, where faulting in the 1969 M_w 6.1 and 6.6 Pariahuanca earthquakes
612 was compressional [Philip and Megard, 1977; Suarez et al., 1983; Sébrier et al., 1988] (see PH1969; Fig.
613 1a). However, both north and south of Shira, where the foreland has wide and active thin-skinned
614 fold-thrust belts [Kley et al., 1999], the high Andes are undergoing extension [Heim, 1949; Doser, 1987;
615 Devlin et al., 2012, This study] (Figs. 1a, 13).

616 It is possible that once the Andes reached the maximum elevation that could be supported by

617 the steep reverse faults bounding the eastern edge of the range $\sim 5\text{-}9$ Ma (Fig. 14a), the plateau
618 widened as faulting propagated eastward into the thick foreland basin sediments that had accumulated
619 concomitant with uplift [e.g. Molnar and Lyon-Caen, 1989]. Foreland deformation then became focused
620 along weak detachment layers above the sediment-basement interface, and the rigid Brazilian Shield
621 was underthrust further beneath the mountains [Kley et al., 1999; Lamb, 2006, 2011; Phillips et al.,
622 2012] (Fig. 14b). As the force balance in the eastern Andes is controlled by the horizontal shear
623 stresses acting on the base of the overriding lithosphere [e.g. Huppert, 1982; McKenzie et al., 2000],
624 reducing the frictional shear stresses along the nose of the foreland fold-thrust belt would be balanced
625 by extensional viscous strain and normal-faulting within the overriding lithosphere (see the calculations
626 presented in Craig and Copley [2018]). In addition to the onset of extension within the high Andes,
627 the ductile lower crust in front of the indenting foreland lithosphere would shorten and thicken [Barke
628 and Lamb, 2006; Lamb, 2011], balancing the flux of material out over the South American foreland.
629 At the surface this would be visible as the mountains spreading eastwards over the forelands coeval
630 with extension in the highest parts of the range - a feature that is reflected in the current pattern of
631 crustal deformation (Fig. 14b).

632 Previous models of the dynamics in the Andes have typically treated the mountain belt in terms
633 of vertically-averaged stress and strain (i.e. a thin-viscous sheet) [Lamb, 2000; Liu et al., 2002; Flesch
634 and Kreemer, 2010]. Under the thin-sheet assumptions shear stresses on the base of the lithosphere
635 are negligible, and weakening the eastern side of the Andes would simply enhance shortening strain
636 rates in that region to maintain the horizontal force balance. Our insight is to include the influence of
637 the underthrust South American foreland, which will partition the force balance with depth beneath
638 the mountains (i.e. F_u and F_p in Fig. 14b), and accommodate extension of the upper crust in the
639 Andes.

640 5.3 Implications for the Evolution of Orogenic Belts

641 A generalisation of the model presented above, in which mountain belts weaken their forelands through
642 syn-orogenic sedimentation, is likely to be broadly applicable to orogen evolution [e.g. Lamb, 2006;
643 Copley et al., 2009; Reynolds et al., 2015]. For example, the deformation style within the forelands
644 of the Tien Shan is dependent on the thickness of the sedimentary basins bounding the basement
645 uplifts [Kober et al., 2013]. Along range fronts adjacent to thick (10-15 km) sedimentary basins,
646 anticlinal folding above buried reverse faults extends ~ 30 km into the piedmont, suggesting shortening
647 is beginning to step out from the basement-cutting faults onto low-angle detachments in the foreland
648 stratigraphy [Avouac and Tapponnier, 1993]. However in regions where the basin sediments are thin

649 (<5 km), faulting has remained focused along steep reverse faults that outcrop at the range front
650 [Avouac and Tapponnier, 1993]. Quaternary-Holocene fault scarps [Thompson et al., 2002], and
651 recent seismicity [Sloan et al., 2011], indicate shortening is still active throughout the interior of the
652 Tien Shan, which probably reflects the fact that the steep, basement-cutting reverse faults can still
653 transmit enough force into the mountain range to overcome the gravitational body forces acting to
654 drive extension.

655 In contrast, within the southern forelands of Tibet, deformation has focused onto detachment hori-
656 zons that cut through the foreland stratigraphy, and emerge ~80-100 km south of the high Himalaya
657 [Lavé and Avouac, 2000]. Geomorphic evidence for uplift [Lavé and Avouac, 2000], and the pattern of
658 shortening reflected in thrust-faulting earthquakes [Molnar and Lyon-Caen, 1989], is confined to the
659 edges of the mountain belt, whilst extension occurs simultaneously in the high plateau [Armijo et al.,
660 1986]. Tibet therefore represents a more advanced stage of orogen evolution, similar to the Altiplano,
661 in which shortening has localised into the sediments of the foreland basin.

662 In summary, we suggest the mechanical properties and nature of the stratigraphy within foreland
663 basins may be important in modulating the forces transmitted across the forelands, the stress field
664 within orogenic belts, and the elevation that mountain belts can attain.

665 6 Conclusions

666 We have used InSAR, seismology and field observations to determine a source model for the 1st
667 December 2016 M_w 6.1 Parina earthquake in the high Andes of south Peru. Our models suggest
668 the earthquake was generated by slip on a shallow-crustal normal fault that accommodated NE-SW
669 extension. Slip in the earthquake was partially buried, and around 15-35% of the shallow co-seismic
670 slip deficit was accommodated by post-seismic afterslip within 6 months of the event.

671 We find that extension in the Parina earthquake was parallel to the direction of shortening across
672 the adjacent sub-Andean lowlands, and that the pattern of shortening in the sub-Andes is controlled
673 by gradients in the topography. In addition, we find that normal faulting earthquakes and geomorpho-
674 logical evidence for recent extensional deformation within the Andes concentrates in regions with the
675 highest elevations. All of these observations imply forces generated by lateral contrasts in gravitational
676 potential energy are important in controlling deformation in the high Andes and its eastern lowlands.

677 We calculated the force per unit length exerted between the Andes and its forelands due to varia-
678 tions in gravitational potential energy to be $4 - 8 \times 10^{12}$ N per metre along-strike. Earthquakes within
679 the South American forelands > 300 km from the Andes range front suggest the crust is breaking
680 in response to these forces, which requires the foreland faults have an effective coefficient of friction

681 $\lesssim 0.2$, and support average shear stresses $\lesssim 110$ MPa. Within 300 km of the Andes range front the
682 extensional stresses in the shallow, bending portion of the foreland lithosphere are large enough to
683 break faults. Using estimates of the curvature of the South American foreland and the rheology of
684 the lithosphere, we can place similar upper bounds on the magnitude of the shear stresses acting on
685 faults in the bending South American forelands ($\lesssim 90$ -130 MPa).

686 Normal faulting in the Andes began in the late Miocene following a period of orogen-wide com-
687 pression, which reflects a change in the force balance across the mountain range. The coeval onset of
688 low-angle detachment faulting in the sub-Andes and extension in the high Andes ~ 5 -9 Ma, in addition
689 to the spatial correlation between extension in the high mountains and wide thin-skinned fold-thrust
690 belts in the adjacent sub-Andes, suggests weak detachment horizons in the foreland stratigraphy could
691 have reduced the forces transmitted into the mountain belt by shear stresses along the base of the
692 overriding lithosphere, leading to the onset of extension in the high mountains. The dynamics and
693 evolution of the Andes, and we suggest most mountain ranges, may therefore be influenced by the
694 mechanical strength of the stratigraphy in its forelands.

695 7 Acknowledgements

696 This work forms part of the NERC- and ESRC-funded project ‘Earthquakes without Frontiers’, and
697 was partly supported by the NERC large grant ‘Looking into Continents from Space’. CB and EA
698 wish to acknowledge INGEMMET and Cusco-PATA (Nú006-2016-FONDECYT) for support of the
699 fieldwork. SW was partly supported by the British Geological Survey. SW thanks Marcelo Assumpção
700 for providing the crustal thickness measurements, in addition to Lorcan Kennan, Christoph Grützner
701 and James Jackson for discussions. The authors thank Peter Molnar, Robert Smalley and particularly
702 Simon Lamb for constructive reviews. Figures were drafted using the free software Generic Mapping
703 Tools [Wessel et al., 2013]. All data used in this study are open access and freely available. InSAR data
704 was collected from the ESA Copernicus Hub (<https://scihub.copernicus.eu/>), seismic data was
705 downloaded from the IRIS data management centre (http://ds.iris.edu/wilber3/find_event)
706 and Landsat data was collected from EarthExplorer (<https://earthexplorer.usgs.gov/>).

707 A Derivation of Relaxation Time-scale for Elevation Contrasts

708 Consider two uniform columns of isostatically-compensated lithosphere with constant viscosity η ,
 709 thickness L_1 and L_2 separated by a height difference h . A simple 1-D horizontal force balance between
 710 body forces acting on the columns and viscous resistance, assuming shear stresses on horizontal planes
 711 are negligible, is given by [D’Agostino et al., 2012; England and Molnar, 2015]:

$$2L \frac{\partial \tau_{xx}}{\partial x} = \frac{\partial \Gamma}{\partial x}, \quad (\text{A.1})$$

712 where τ_{xx} is the vertically-averaged deviatoric stress acting on the columns and Γ is the gravitational
 713 potential energy per unit area of the column. Assuming the columns are Newtonian (i.e. $\tau_{xx} = 2\eta\dot{\epsilon}_{xx}$)
 714 and integrating Eq. A.1 yields:

$$\dot{\epsilon}_{xx} = \frac{\Delta\Gamma}{4\eta L}, \quad (\text{A.2})$$

715 where $\Delta\Gamma$ is the difference in gravitational potential energy between a column with zero strain rate
 716 (i.e. undeforming) and the column in question. For Airy isostatic compensation $\Delta\Gamma$ can be expressed
 717 approximately as γh , where γ is some constant scaling elevation contrasts between the deforming and
 718 undeforming area (h) to the gravitational potential energy contrast [D’Agostino et al., 2014]. In our
 719 case, one of the columns (i.e. the Bolivian Altiplano) is assumed to be undeforming, therefore the
 720 strain rate in the deforming column (i.e. south Peru) is proportional to the elevation of that column
 721 above the undeforming column.

722 Assuming incompressibility of each column of lithosphere, and the conservation of area in cross
 723 section, horizontal extension of the column at strain rate $\dot{\epsilon}_{xx}$ in response to horizontal contrasts in
 724 gravitational potential energy would lead to thinning given by:

$$\frac{dL}{dt} = -\dot{\epsilon}_{xx}L = -\frac{\gamma h}{4\eta} \quad (\text{A.3})$$

725 The difference in the thickness of the higher, deforming column and the undeforming column
 726 $L_1 - L_2$ is related to the elevation contrast through an isostatic relationship $L_1 - L_2 = h \frac{\rho_m}{\Delta\rho}$, where
 727 $\Delta\rho$ is the density difference between mantle and crust. Substituting the isostatic relationship into Eq.
 728 A.3 gives the following first order ODE:

$$\frac{dh}{dt} + \frac{\gamma\Delta\rho}{4\eta\rho_m}h = 0 \quad (\text{A.4})$$

729 This equation has a particular solution of the form $h(t) = h_0 \exp(-t/t_r)$, where $t_r = \frac{4\eta\rho_m}{\gamma\Delta\rho}$ and h_0

730 is the starting elevation of the deforming column above the undeforming column. Therefore the
731 elevation contrasts between deforming and undeforming regions within a mountain belt will decay
732 exponentially at a rate dependent on the density contrasts between crust and mantle and the viscosity
733 of the lithosphere.

734 Given the maximum possible extensional strain rate in south Peru as $2 \times 10^{-8} \text{ yr}^{-1}$, γ as 1.5×10^9
735 N m^{-1} per metre of elevation (see calculations in Section 4.1), h as 700 m and L as 150 km, we can use
736 Eq. A.2 to compute a lower bound on the viscosity, which is $\eta > 3 \times 10^{21} \text{ Pa s}$. Our lower bound on
737 the viscosity of the lithosphere is consistent with Lamb [2000], who infer the average viscosity of the
738 lithosphere in the Andes is $5 - 10 \times 10^{21} \text{ Pa s}$. Taking ρ_m and ρ_c as 3300 and 2800 kg m^{-3} , respectively,
739 the relaxation time-scale of elevation contrasts would be $t_r > 3 \text{ Myrs}$. Under constant force boundary
740 conditions, after $>9 \text{ Myrs}$ around 95% of the elevation contrasts between south Peru and Bolivia will
741 have been removed via extension. We therefore infer that the elevation contrasts between south Peru
742 and Bolivia are unlikely to have existed for $\gg 10 \text{ Myrs}$.

References

- Alvarado, P. and Beck, S. (2006). Source characterization of the San Juan (Argentina) crustal earthquakes of 15 January 1944 (Mw 7.0) and 11 June 1952 (Mw 6.8). *Earth and Planetary Science Letters*.
- Armijo, R., Tapponnier, P., Mercier, J. L., and Han, T.-L. (1986). Quaternary extension in southern Tibet: Field observations and tectonic implications. *Journal of Geophysical Research*, 91:13803.
- Artyushkov, E. V. (1973). Stresses in the lithosphere caused by crustal thickness inhomogeneities. *Journal of Geophysical Research*, 78(32):7675–7708.
- Assumpção, M. (1992). The Regional Intraplate Stress Field in South America. *Journal of Geophysical Research*, 97903(11):889–11.
- Assumpção, M. and Araujo, M. (1993). Effect of the Altiplano-Puna plateau, South America, on the regional intraplate stresses. *Tectonophysics*, 221(3-4):475–496.
- Assumpção, M., Feng, M., Tassara, A., and Julià, J. (2013). Models of crustal thickness for South America from seismic refraction, receiver functions and surface wave tomography. *Tectonophysics*, 609:82–96.
- Assumpção, M. and Suarez, G. (1988). Source mechanisms of moderate-size earthquakes and stress orientation in mid-plate South America. *Geophysical Journal*, 92(2):253–267.
- Avouac, J. and Tapponnier, P. (1993). Kinematic model of active deformation in central Asia. *Geophysical Research Letters*, 20(10):895.
- Babeyko, A. Y., Sobolev, S. V., Vietor, T., Oncken, O., and Trumbull, R. B. (2006). Numerical Study of Weakening Processes in the Central Andean Back-Arc. In Oncken, O., editor, *The Andes - Active Subduction Orogeny*, pages 495–512. Springer Berlin Heidelberg.
- Barke, R. and Lamb, S. (2006). Late Cenozoic uplift of the Eastern Cordillera, Bolivian Andes. *Earth and Planetary Science Letters*, 249(3-4):350–367.
- Beck, S. L. and Zandt, G. (2002). The nature of orogenic crust in the central Andes. *Journal of Geophysical Research: Solid Earth*, 107(B10):ESE 7–1–ESE 7–16.
- Benavente, C., Zerathe, S., Audin, L., Hall, S. R., Robert, X., Delgado, F., Carcaillet, J., and Team, A. (2017). Active transpressional tectonics in the Andean forearc of southern Peru quantified by ^{10}Be surface exposure dating of an active fault scarp. *Tectonics*, 36(9):1662–1678.

- Benavente, E. C., Delgado, M. F., Taibe, M. E., Audin, L., and Pari, W. (2013). Neotectonica y Peligro Sismico en el Region Cusco. Technical report, Instituto Geologico Minera y Metalurgico.
- Bevis, M., Kendrick, E., Smalley, R., Brooks, B., Allmendinger, R., and Isacks, B. (2001). On the strength of interplate coupling and the rate of back arc convergence in the central Andes: An analysis of the interseismic velocity field. *Geochemistry, Geophysics, Geosystems*, 2(11):n/a–n/a.
- Bevis, M. and Martel, S. J. (2001). Oblique plate convergence and interseismic strain accumulation. *Geochemistry Geophysics Geosystems*, 2(8):art. no.–2000GC000125.
- Bie, L., Ryder, I., Nippres, S. E. J., and Burgmann, R. (2014). Coseismic and post-seismic activity associated with the 2008 Mw 6.3 Damxung earthquake, Tibet, constrained by InSAR. *Geophysical Journal International*, 196(2):788–803.
- Bouhifd, M. a., Andrault, D., Fiquet, G., and Richet, P. (1996). Thermal expansion of forsterite up to the melting point . *Geophysical Research Letters*, 23(10):1143–1146.
- Brace, W. F. and Kohlstedt, D. L. (1980). Limits on lithospheric stress imposed by laboratory experiments. *Journal of Geophysical Research: Solid Earth*, 85(B11):6248–6252.
- Brune, J. N. (1968). Seismic moment, seismicity, and rate of slip along major fault zones. *Journal of Geophysical Research*, 73(2):777–784.
- Bry, M. and White, N. (2007). Reappraising elastic thickness variation at oceanic trenches. *Journal of Geophysical Research*, 112(B8):B08414.
- Byerlee, J. (1978). Friction of rocks. *Pure and Applied Geophysics*, 116(4-5):615–626.
- Cabrera, J. and Sebrier, M. (1998). Surface Rupture Associated with a 5.3-mb Earthquake: The 5 April 1986 Cuzco Earthquake and Kinematics of the Chincheros-Qoricocha Faults of the High Andes, Peru. *Bulletin of the Seismological Society of America*, 88(1):242–255.
- Cabrera, J., Sébrier, M., and Mercier, J. L. (1991). Plio-Quaternary geodynamic evolution of a segment of the Peruvian Andean Cordillera located above the change in the subduction geometry: the Cuzco region. *Tectonophysics*, 190(2-4):331–362.
- Chapman, C. H. (1978). A new method for computing synthetic seismograms. *Geophysical Journal International*, 54(3):481–518.

- Chen, C. W. and Zebker, H. A. (2001). Two-dimensional phase unwrapping with use of statistical models for cost functions in nonlinear optimization. *Journal of the Optical Society of America A*, 18(2):338.
- Chinn, D. S. and Isacks, B. L. (1983). Accurate source depths and focal mechanisms of shallow earthquakes in western South America and in the New Hebrides Island Arc. *Tectonics*, 2(6):529–563.
- Chlieh, M., Perfettini, H., Tavera, H., Avouac, J.-P., Remy, D., Nocquet, J.-M., Rolandone, F., Bondoux, F., Gabalda, G., and Bonvalot, S. (2011). Interseismic coupling and seismic potential along the Central Andes subduction zone. *Journal of Geophysical Research*, 116(B12):B12405.
- Cladouhos, T. T., Allmendinger, R. W., Coira, B., and Farrar, E. (1994). Late cenozoic deformation in the Central Andes: fault kinematics from the northern Puna, northwestern Argentina and southwestern Bolivia. *Journal of South American Earth Sciences*, 7(2):209–228.
- Clapperton, C. (1983). The glaciation of the Andes. *Quaternary Science Reviews*, 2(2-3):83–155.
- Collettini, C., Niemeijer, A., Viti, C., and Marone, C. (2009). Fault zone fabric and fault weakness. *Nature*, 462(7275):907–910.
- Copley, A. (2012). The formation of mountain range curvature by gravitational spreading. *Earth and Planetary Science Letters*, 351-352:208–214.
- Copley, A., Avouac, J.-P., Hollingsworth, J., and Leprince, S. (2011a). The 2001 Mw 7.6 Bhuj earthquake, low fault friction, and the crustal support of plate driving forces in India. *Journal of Geophysical Research*, 116(B8):B08405.
- Copley, A., Avouac, J.-P., and Wernicke, B. P. (2011b). Evidence for mechanical coupling and strong Indian lower crust beneath southern Tibet. *Nature*, 472(7341):79–81.
- Copley, A., Boait, F., Hollingsworth, J., Jackson, J., and McKenzie, D. (2009). Subparallel thrust and normal faulting in Albania and the roles of gravitational potential energy and rheology contrasts in mountain belts. *Journal of Geophysical Research*, 114(B5):B05407.
- Copley, A., Karasozen, E., Oveisi, B., Elliott, J. R., Samsonov, S., and Nissen, E. (2015). Seismogenic faulting of the sedimentary sequence and laterally variable material properties in the Zagros Mountains (Iran) revealed by the August 2014 Murmuri (E. Dehloran) earthquake sequence. *Geophysical Journal International*, 203(2):1436–1459.

- Copley, A. and McKenzie, D. (2007). Models of crustal flow in the India-Asia collision zone. *Geophysical Journal International*, 169(2):683–698.
- Copley, A. and Woodcock, N. (2016). Estimates of fault strength from the Variscan foreland of the northern UK. *Earth and Planetary Science Letters*, 451:108–113.
- Craig, T. J. and Copley, A. (2018). Forearc collapse, plate flexure, and seismicity within the downgoing plate along the Sunda Arc west of Sumatra. *Earth and Planetary Science Letters*, 484:81–91.
- Craig, T. J., Copley, A., and Jackson, J. (2012). Thermal and tectonic consequences of India underthrusting Tibet. *Earth and Planetary Science Letters*, 353-354:231–239.
- Craig, T. J., Jackson, J. a., Priestley, K., and McKenzie, D. (2011). Earthquake distribution patterns in Africa: their relationship to variations in lithospheric and geological structure, and their rheological implications. *Geophysical Journal International*, 185(1):403–434.
- D’Agostino, N., Cheloni, D., Fornaro, G., Giuliani, R., and Reale, D. (2012). Space-time distribution of afterslip following the 2009 L’Aquila earthquake. *Journal of Geophysical Research: Solid Earth*, 117(B2):n/a–n/a.
- D’Agostino, N., England, P., Hunstad, I., and Selvaggi, G. (2014). Gravitational potential energy and active deformation in the Apennines. *Earth and Planetary Science Letters*, 397:121–132.
- Dalmayrac, B. and Molnar, P. (1981). Parallel thrust and normal faulting in Peru and constraints on the state of stress. *Earth and Planetary Science Letters*, 55(3):473–481.
- Daxberger, H. and Riller, U. (2015). Kinematics of Neogene to Recent upper-crustal deformation in the southern Central Andes (23-28S) inferred from fault-slip analysis: Evidence for gravitational spreading of the Puna Plateau. *Tectonophysics*, 642(1):16–28.
- DeMets, C., Gordon, R. G., Argus, D. F., M.M., W., F.H., W., J.B., J., E., P., and R., S. (2010). Geologically current plate motions. *Geophysical Journal International*, 181(1):1–80.
- Devlin, S., Isacks, B. L., Pritchard, M. E., Barnhart, W. D., and Lohman, R. B. (2012). Depths and focal mechanisms of crustal earthquakes in the central Andes determined from teleseismic waveform analysis and InSAR. *Tectonics*, 31(2):1–33.
- Dorbath, C. (1996). Velocity structure of the Andes of central Peru from locally recorded earthquakes. *Geophysical Research Letters*, 23(2):205–208.

- Doser, D. I. (1987). The Ancash, Peru, earthquake of 1946 November 10: evidence for low-angle normal faulting in the high Andes of northern Peru. *Geophysical Journal of the Royal Astronomical Society*, 91(1):57–71.
- Dziewonski, A. M., Chou, T.-A., and Woodhouse, J. H. (1981). Determination of earthquake source parameters from waveform data for studies of global and regional seismicity. *Journal of Geophysical Research: Solid Earth*, 86(B4):2825–2852.
- Echavarría, L., Hernández, R., Allmendinger, R., and Reynolds, J. (2003). Subandean thrust and fold belt of northwestern Argentina: Geometry and timing of the Andean evolution. *AAPG Bulletin*, 87(6):965–985.
- Ekström, G., Nettles, M., and Dziewoński, A. (2012). The global CMT project 20042010: Centroid-moment tensors for 13,017 earthquakes. *Physics of the Earth and Planetary Interiors*, 200:1–9.
- Elger, K., Oncken, O., and Glodny, J. (2005). Plateau-style accumulation of deformation: Southern Altiplano. *Tectonics*, 24(4):1–19.
- Ellison, R., Klinck, B., and Hawkins, M. (1989). Deformation events in the Andean orogenic cycle in the Altiplano and Western Cordillera, southern Peru. *Journal of South American Earth Sciences*, 2(3):263–276.
- Emmerson, B. (2007). *The relationship between intraplate earthquakes and temperature*. PhD thesis, University of Cambridge.
- Engdahl, E. R., van der Hilst, R., and Buland, R. (1998). Global Teleseismic Earthquake Relocation with Improved Travel Times and Procedures for Depth Determination. *Bulletin of the Seismological Society of America*, 88(3):722–743.
- England, P. and Houseman, G. (1989). Extension during continental convergence, with application to the Tibetan Plateau. *Journal of Geophysical Research*, 94(B12):17561.
- England, P. and McKenzie, D. (1982). A thin viscous sheet model for continental deformation. *Geophysical Journal International*, 70(2):295–321.
- England, P. and Molnar, P. (1997). Active Deformation of Asia: From Kinematics to Dynamics. *Science*, 278(5338).
- England, P. and Molnar, P. (2015). Rheology of the lithosphere beneath the central and western Tien Shan. *Journal of Geophysical Research: Solid Earth*, 120(5):3803–3823.

- Espurt, N., Brusset, S., Baby, P., Hermoza, W., Bolaños, R., Uyen, D., and Déramond, J. (2008). Paleozoic structural controls on shortening transfer in the Subandean foreland thrust system, Ene and southern Ucayali basins, Peru. *Tectonics*, 27(3):1–21.
- Farr, T. G., Rosen, P. A., Caro, E., Crippen, R., Duren, R., Hensley, S., Kobrick, M., Paller, M., Rodriguez, E., Roth, L., Seal, D., Shaffer, S., Shimada, J., Umland, J., Werner, M., Oskin, M., Burbank, D., and Alsdorf, D. (2007). The Shuttle Radar Topography Mission. *Reviews of Geophysics*, 45(2):RG2004.
- Fialko, Y., Sandwell, D., Simons, M., and Rosen, P. (2005). Three-dimensional deformation caused by the Bam, Iran, earthquake and the origin of shallow slip deficit. *Nature*, 435(7040):295–299.
- Fielding, E. J., Lundgren, P. R., Bürgmann, R., and Funning, G. J. (2009). Shallow fault-zone dilatancy recovery after the 2003 Bam earthquake in Iran. *Nature*, 458(7234):64–68.
- Flesch, L. M. and Kreemer, C. (2010). Gravitational potential energy and regional stress and strain rate fields for continental plateaus: Examples from the central Andes and Colorado Plateau. *Tectonophysics*, 482(1-4):182–192.
- Froidevaux, C. and Isacks, B. L. (1984). The mechanical state of the lithosphere in the Altiplano-Puna segment of the Andes. *Earth and Planetary Science Letters*, 71(2):305–314.
- Funning, G. J., Barke, R. M. D., Lamb, S. H., Minaya, E., Parsons, B., and Wright, T. J. (2005). The 1998 Aiquile, Bolivia earthquake: A seismically active fault revealed with InSAR. *Earth and Planetary Science Letters*, 232(1-2):39–49.
- Garzzone, C. N., Hoke, G. D., Libarkin, J. C., Withers, S., MacFadden, B., Eiler, J., Ghosh, P., and Mulch, A. (2008). Rise of the Andes. *Science (New York, N.Y.)*, 320(5881):1304–1307.
- Garzzone, C. N., McQuarrie, N., Perez, N. D., Ehlers, T. A., Beck, S. L., Kar, N., Eichelberger, N., Chapman, A. D., Ward, K. M., Ducea, M. N., Lease, R. O., Poulsen, C. J., Wagner, L. S., Saylor, J. E., Zandt, G., and Horton, B. K. (2017). Tectonic Evolution of the Central Andean Plateau and Implications for the Growth of Plateaus. *Annual Review of Earth and Planetary Sciences*, 45(1):annurev-earth-063016-020612.
- Garzzone, C. N., Molnar, P., Libarkin, J. C., and MacFadden, B. J. (2006). Rapid late Miocene rise of the Bolivian Altiplano: Evidence for removal of mantle lithosphere. *Earth and Planetary Science Letters*, 241(3-4):543–556.

- Gautheron, C., Espurt, N., Barbarand, J., Roddaz, M., Baby, P., Brusset, S., Tassan-Got, L., and Douville, E. (2013). Direct dating of thick- and thin-skin thrusts in the Peruvian Subandean zone through apatite (U-Th)/He and fission track thermochronometry. *Basin Research*, 25(4):419–435.
- Giovanni, M. K., Horton, B. K., Garzzone, C. N., McNulty, B., and Grove, M. (2010). Extensional basin evolution in the Cordillera Blanca, Peru: Stratigraphic and isotopic records of detachment faulting and orogenic collapse in the Andean hinterland. *Tectonics*, 29(6):1–21.
- Goetze, C. and Evans, B. (1979). Stress and temperature in the bending lithosphere as constrained by experimental rock mechanics. *Geophysical Journal of the Royal Astronomical Society*, 59(3):463–478.
- Goldstein, R. M., Zebker, H. A., and Werner, C. L. (1988). Satellite radar interferometry: Two-dimensional phase unwrapping. *Radio Science*, 23(4):713–720.
- Gubbels, T. L., Isacks, B. L., and Farrar, E. (1993). High-level surfaces, plateau uplift, and foreland development, Bolivian central Andes. *Geology*, 21(8):695.
- Gutscher, M.-A., Spakman, W., Bjiwaard, H., and Enghdahl, E. R. (2000). Geodynamics of flat subduction: Seismicity and tomographic constraints from the Andean margin. *October*, 19(5):814–833.
- Hall, S. R., Farber, D. L., Audin, L., and Finkel, R. C. (2012). Recently active contractile deformation in the forearc of southern Peru. *Earth and Planetary Science Letters*, 337-338:85–92.
- Heim, A. (1949). Observaciones Geologicas en La Region del Terremoto de Ancash de Noviembre de 1946. Technical report, Sociada Geologica del Peru.
- Hoke, L. and Lamb, S. (2007). Cenozoic behind-arc volcanism in the Bolivian Andes, South America: implications for mantle melt generation and lithospheric structure. *Journal of the Geological Society*, 164(4).
- Holtkamp, S. G., Pritchard, M. E., and Lohman, R. B. (2011). Earthquake swarms in South America. *Geophysical Journal International*, 187(1):128–146.
- Huppert, H. E. (1982). Propagation of two-dimensional and axisymmetric viscous gravity currents over a rigid horizontal surface. *Journal of Fluid Mechanics*, 121:43–58.
- Husson, L. and Ricard, Y. (2004). Stress balance above subduction: Application to the Andes. *Earth and Planetary Science Letters*, 222(3-4):1037–1050.

- Imber, J., Holdsworth, R. E., Smith, S. A. F., Jefferies, S. P., and Collettini, C. (2008). Frictional-viscous flow, seismicity and the geology of weak faults: a review and future directions. *Geological Society, London, Special Publications*, 299(1):151–173.
- Ingleby, T. and Wright, T. J. (2017). Omorilike decay of postseismic velocities following continental earthquakes. *Geophysical Research Letters*, 44(7):3119–3130.
- Jackson, J., McKenzie, D., Priestley, K., and Emmerson, B. (2008). New views on the structure and rheology of the lithosphere. *Journal of the Geological Society*, 165(2):453–465.
- Jackson, J., Priestley, K., Allen, M., and Berberian, M. (2002). Active tectonics of the South Caspian Basin. *Geophysical Journal International*, 148(2):214–245.
- Jackson, J. A. and White, N. J. (1989). Normal faulting in the upper continental crust: observations from regions of active extension. *Journal of Structural Geology*, 11(1-2):15–36.
- Jackson, J. A. J., Gagnepain, J., Houseman, G., King, G. C. P., Papadimitriou, P., Soufleris, C., and Viriueux, J. (1982). Seismicity, normal faulting, and the geomorphological development of the Gulf of Corinth (Greece): the Corinth earthquakes of February and March 1981. *Earth and Planetary Science Letters*, 57(2):377–397.
- Jackson, M. and Blenkinsop, T. (1997). The Bilila-Mtakataka fault in Malai: An active, 100-km long, normal fault segment in thick seismogenic crust. *Tectonics*, 16(1):137–150.
- Jay, J. A., Delgado, F. J., Torres, J. L., Pritchard, M. E., Macedo, O., and Aguilar, V. (2015). Deformation and seismicity near Sabancaya volcano, southern Peru, from 2002 to 2015. *Geophysical Research Letters*, 42(8):2780–2788.
- Kadinsky-Cade, K., Reilinger, R., and Isacks, B. (1985). Surface deformation associated with the November 23, 1977, Caucete, Argentina, earthquake sequence. *J. Geophys. Res.*, 90:12691–12700.
- Kaneko, Y. and Fialko, Y. (2011). Shallow slip deficit due to large strike-slip earthquakes in dynamic rupture simulations with elasto-plastic off-fault response. *Geophysical Journal International*, 186(3):1389–1403.
- Kar, N., Garziona, C. N., Jaramillo, C., Shanahan, T., Carlotto, V., Pullen, A., Moreno, F., Anderson, V., Moreno, E., and Eiler, J. (2016). Rapid regional surface uplift of the northern Altiplano plateau revealed by multiproxy paleoclimate reconstruction. *Earth and Planetary Science Letters*, 447:33–47.

- Karato, S.-i. and Wu, P. (1993). Rheology of the Upper Mantle: A Synthesis. *Science*, 260(5109).
- Kay, R. and Mahlburg Kay, S. (1993). Delamination and delamination magmatism. *Tectonophysics*, 219(1-3):177–189.
- Kendrick, E., Bevis, M., and Brooks, B. (2001). An integrated crustal velocity field for the central Andes. *Geochemistry Geophysics Geosystems*, 2.
- Kennan, L. (1993). Cenezoic Evolution of the Cochabamba Area, Bolivia. In *Second ISAG*, pages 21–23, Oxford.
- Kennett, B. L. N., Engdahl, E. R., and Buland, R. (1995). Constraints on seismic velocities in the Earth from traveltimes. *Geophysical Journal International*, 122(1):108–124.
- Kley, J. (1996). Transition from basement-involved to thin-skinned thrusting in the Cordillera Oriental of southern Bolivia. *Tectonics*, 15(4):763–775.
- Kley, J. and Monaldi, C. R. (1998). Tectonic shortening and crustal thickness in the Central Andes: How good is the correlation? *Geology*, 26(8):723–726.
- Kley, J., Monaldi, C. R., and Salfity, J. A. (1999). Along-strike segmentation of the Andean foreland: Causes and consequences. *Tectonophysics*, 301(1-2):75–94.
- Kober, M., Seib, N., Kley, J., and Voigt, T. (2013). Thick-skinned thrusting in the northern Tien Shan foreland, Kazakhstan: structural inheritance and polyphase deformation. *Geological Society, London, Special Publications*, 377(1):19–42.
- Lamb, S. (2006). Shear stresses on megathrusts: Implications for mountain building behind subduction zones. *Journal of Geophysical Research*, 111(B7):B07401.
- Lamb, S. (2011). Did shortening in thick crust cause rapid Late Cenozoic uplift in the northern Bolivian Andes? *Journal of the Geological Society*, 168(5):1079–1092.
- Lamb, S. (2016). Cenozoic uplift of the Central Andes in northern Chile and Bolivia reconciling paleoaltimetry with the geological evolution. *Canadian Journal of Earth Sciences*, 53(11):1227–1245.
- Lamb, S. and Hoke, L. (1997). Origin of the high plateau in the Central Andes, Bolivia, South America. *Journal of Geophysical Research*, 102(4):623–649.
- Lamb, S. H. (2000). Active deformation in the Bolivian Andes, South America. *Journal of Geophysical Research*, 105(B11):25627–25653.

- Lavé, J. and Avouac, J. P. (2000). Active folding of fluvial terraces across the Siwaliks Hills, Himalayas of central Nepal. *Journal of Geophysical Research: Solid Earth*, 105(B3):5735–5770.
- Lavenu, A., Thiele, R., Machette, M., Dart, R., Lee-Ann, B., and Haller, K. (2000). Maps and Database of Quaternary Faults in Bolivia and Chile. Technical report, United States Geological Survey.
- Lin, Y. N. N., Sladen, A., Ortega-Culaciati, F., Simons, M., Avouac, J. P., Fielding, E. J., Brooks, B. A., Bevis, M., Genrich, J., Rietbrock, A., Vigny, C., Smalley, R., and Socquet, A. (2013). Coseismic and postseismic slip associated with the 2010 Maule Earthquake, Chile: Characterizing the Arauco Peninsula barrier effect. *Journal of Geophysical Research: Solid Earth*, 118(6):3142–3159.
- Liu, M., Yang, Y., Stein, S., and Klosko, E. (2002). Crustal Shortening and Extension in the Central Andes: Insights from a Viscoelastic Model. *Plate Boundary Zones*, pages 325–339.
- Lucassen, F., Franz, G., Viramonte, J., Romer, R. L., Dulski, P., and Lang, A. (2005). The late Cretaceous lithospheric mantle beneath the Central Andes: Evidence from phase equilibria and composition of mantle xenoliths. *Lithos*, 82(3-4 SPEC. ISS.):379–406.
- Lucassen, F., Lewerenz, S., Franz, G., Viramonte, J., and Mezger, K. (1999). Metamorphism, isotopic ages and composition of lower crustal granulite xenoliths from the Cretaceous Salta Rift, Argentina. *Contributions to Mineralogy and Petrology*, 134(4):325–341.
- Lyon-Caen, H., Molnar, P., and Suárez, G. (1985). Gravity anomalies and flexure of the Brazilian Shield beneath the Bolivian Andes. *Earth and Planetary Science Letters*, 75(1):81–92.
- Maggi, a., Jackson, J. a., McKenzie, D., and Priestley, K. (2000a). Earthquake focal depths, effective elastic thickness, and the strength of the continental lithosphere. *Geology*, 28(6):495.
- Maggi, A., Jackson, J. A., Priestley, K., and Baker, C. (2000b). A re-assessment of focal depth distributions in southern Iran, the Tien Shan and northern India: do earthquakes really occur in the continental mantle? *Geophysical Journal International*, 143(3):629–661.
- Margirier, A., Audin, L., Robert, X., Pêcher, A., and Schwartz, S. (2017). Stress field evolution above the Peruvian flat-slab (Cordillera Blanca, northern Peru). *Journal of South American Earth Sciences*, 77:58–69.
- Marone, C. and Scholz, C. H. (1988). The depth of seismic faulting and the upper transition from stable to unstable slip regimes. *Geophysical Research Letters*, 15(6):621–624.

- Marrett, R. A., Allmendinger, R. W., Alonso, R. N., and Drake, R. E. (1994). Late Cenozoic tectonic evolution of the Puna Plateau and adjacent foreland, northwestern Argentine Andes. *Journal of South American Earth Sciences*, 7(2):179–207.
- McCaffrey, R. and Abers, G. (1988). Syn3: a program for inversion of teleseismic body waveforms on microcomputers.
- McCaffrey, R., Abers, G., and Zwick, P. (1991). Inversion of teleseismic body waves. In *IASPEI Software Library*, chapter 3. IASPEI Software Library, 3 edition.
- McGroder, M. F., Lease, R. O., and Pearson, D. M. (2015). Along-strike variation in structural styles and hydrocarbon occurrences, Subandean fold-and-thrust belt and inner foreland, Colombia to Argentina. In DeCelles, P. G., Ducea, M. N., Carrapa, B., and Kapp, P. A., editors, *Geodynamics of a Cordilleran Orogenic System: The Central Andes of Argentina and Northern Chile*. Geological Society of America.
- McKenzie, D. and Fairhead, D. (1997). Estimates of the effective elastic thickness of the continental lithosphere from Bouguer and free air gravity anomalies. *Journal of Geophysical Research: Solid Earth*, 102(B12):27523–27552.
- McKenzie, D., Jackson, J., and Priestley, K. (2005). Thermal structure of oceanic and continental lithosphere. *Earth and Planetary Science Letters*, 233(3):337–349.
- McKenzie, D., Nimmo, F., and Jackson, J. A. (2000). Characteristics and Consequences of Flow in The Lower Crust. *Journal of Geophysical Research*, 105(B5):11029–11046.
- McKenzie, D. and Priestley, K. (2008). The influence of lithospheric thickness variations on continental evolution. *Lithos*, 102(1-2):1–11.
- McKenzie, D. and Priestley, K. (2016). Speculations on the formation of cratons and cratonic basins. *Earth and Planetary Science Letters*, 435:94–104.
- McKenzie, D., Yi, W., and Rummel, R. (2014). Estimates of T_e from GOCE Data. *Earth and Planetary Science Letters*, 399:116–127.
- McKenzie, D. P. and Parker, R. L. (1967). The North Pacific: an Example of Tectonics on a Sphere. *Nature*, 216(5122):1276–1280.
- McNulty, B. and Farber, D. (2002). Active detachment faulting above the Peruvian flat slab. *Geology*, 30(6):567–570.

- Megard, F., Noble, D., McKee, E., and Bellon, H. (1984). Multiple pulses of Neogene compressive deformation in the Ayacucho intermontane basin, Andes of central Peru. *Geological Society of America Bulletin*, 95(9):1108.
- Mei, S., Suzuki, A. M., Kohlstedt, D. L., Dixon, N. A., and Durham, W. B. (2010). Experimental constraints on the strength of the lithospheric mantle. *Journal of Geophysical Research*, 115(B8):B08204.
- Meijer, P., Govers, R., and Wortel, M. (1997). Forces controlling the present-day state of stress in the Andes. *Earth and Planetary Science Letters*, 148(1-2):157–170.
- Mercier, J. L. (1981). Extensional-Compressional Tectonics Associated with the Aegean Arc: Comparison with the Andean Cordillera of South Peru - North Bolivia. *Philosophical Transactions of the Royal Society of London A: Mathematical, Physical and Engineering Sciences*, 300(1454).
- Mercier, J. L., Sebrier, M., Lavenu, A., Cabrera, J., Bellier, O., Dumont, J.-F., and Machrare, J. (1992). Changes in the tectonic regime above a subduction zone of Andean Type: The Andes of Peru and Bolivia during the Pliocene-Pleistocene. *Journal of Geophysical Research*, 97(B8):11945.
- Molnar, P., Chen, W.-P., Fitch, T. J., Tapponnier, P., Warsi, W. E. K., and Wu, F. (1977). Structure and Tectonics of the Himalaya: A brief summary of relevant geophysical observations. In *Colloque Internationaux du CNRS, No. 268, Himalaya: Sciences de la Terre*, pages 269–294, Paris. du Centre National de la Recherche Scientifique.
- Molnar, P. and Lyon-Caen, H. (1988). Some simple physical aspects of the support, structure, and evolution of mountain belts. In *Geological Society of America Special Papers*, volume 218, pages 179–208. Geological Society of America.
- Molnar, P. and Lyon-Caen, H. (1989). Fault plane solutions of earthquakes and active tectonics of the Tibetan Plateau and its margins. *Geophysical Journal International*, 99(1):123–154.
- Molnar, P. and Stock, J. M. (2009). Slowing of India's convergence with Eurasia since 20 Ma and its implications for Tibetan mantle dynamics. *Tectonics*, 28(3):n/a–n/a.
- Montero Lopez, M. C., Hongn, F. D., Strecker, M. R., Marrett, R., Seggiaro, R., and Sudo, M. (2010). Late Miocene-early Pliocene onset of N-S extension along the southern margin of the Central Andean Puna Plateau: Evidence from magmatic, geochronological and structural observations. *Tectonophysics*, 494(1-2):48–63.

- Nemati, M., Hollingsworth, J., Zhan, Z., Bolourchi, M. J., and Talebian, M. (2013). Microseismicity and seismotectonics of the South Caspian Lowlands, NE Iran. *Geophysical Journal International*, 193(3):1053–1070.
- Ni, J. and Barazangi, M. (1984). Seismotectonics of the Himalayan Collision Zone: Geometry of the underthrusting Indian Plate beneath the Himalaya. *Journal of Geophysical Research: Solid Earth*, 89(B2):1147–1163.
- Norabuena, E. O., Dixon, T. H., Stein, S., and Harrison, C. G. A. (1999). Decelerating Nazca-South America and Nazca-Pacific Plate motions. *Geophysical Research Letters*, 26(22):3405–3408.
- Okada, Y. (1985). Surface deformation due to shear and tensile faults in a half-space. *Bulletin of the Seismological Society of America*, 75(4):1135–1154.
- Oncken, O., Boutelier, D., Dresen, G., and Schemmann, K. (2012). Strain accumulation controls failure of a plate boundary zone: Linking deformation of the Central Andes and lithosphere mechanics. *Geochemistry, Geophysics, Geosystems*, 13(12).
- Oncken, O., Hindle, D., Kley, J., Elger, K., Victor, P., and Schemmann, K. (2006). Deformation of the Central Andean Upper Plate System Facts, Fiction, and Constraints for Plateau Models. In *The Andes*, pages 3–27. Springer Berlin Heidelberg.
- Peltzer, G., Rosen, P., Rogez, F., and Hudnut, K. (1998). Poroelastic rebound along the Landers 1992 earthquake surface rupture. *Journal of Geophysical Research: Solid Earth*, 103(B12):30131–30145.
- Perez, N., Horton, B., McQuarrie, N., Stubner, K., and Ehlers, T. (2016). Andean shortening, inversion and exhumation associated with thin- and thick-skinned deformation in southern Peru. *Geological Magazine*, 153(5-6):1013–1041.
- Pérez-Gussinyé, M., Lowry, A. R., and Watts, A. B. (2007). Effective elastic thickness of South America and its implications for intracontinental deformation. *Geochemistry, Geophysics, Geosystems*, 8(5):n/a–n/a.
- Philip, H. and Megard, F. (1977). Structural analysis of the superficial deformation of the 1969 Pariahuanca earthquakes (Central Peru). *Tectonophysics*, 38(3-4):259–278.
- Phillips, K., Clayton, R. W., Davis, P., Tavera, H., Guy, R., Skinner, S., Stubailo, I., Audin, L., and Aguilar, V. (2012). Structure of the subduction system in southern Peru from seismic array data. *Journal of Geophysical Research B: Solid Earth*, 117(11):n/a–n/a.

- Priestley, K. and McKenzie, D. (2013). The relationship between shear wave velocity, temperature, attenuation and viscosity in the shallow part of the mantle. *Earth and Planetary Science Letters*, 381:78–91.
- Pritchard, M. E., Norabuena, E. O., Ji, C., Boroschek, R., Comte, D., Simons, M., Dixon, T. H., and Rosen, P. A. (2007). Geodetic, teleseismic, and strong motion constraints on slip from recent southern Peru subduction zone earthquakes. *Journal of Geophysical Research*, 112(B3):B03307.
- Renner, S. and Velasco, C. (2000). Geologia E Hidrogeologia Del Valle Central De Cochabamba. Technical report, German Bolivian Agreement on Groundwater (CABAS).
- Reynolds, K., Copley, a., and Hussain, E. (2015). Evolution and dynamics of a fold-thrust belt: the Sulaiman Range of Pakistan. *Geophysical Journal International*, 201(2):683–710.
- Riller, U., Clark, M. D., Daxberger, H., Doman, D., Lenauer, I., Plath, S., and Santimano, T. (2017). Fault-slip inversions : Their importance in terms of strain , heterogeneity , and kinematics of brittle deformation. *Journal of Structural Geology*, 101:B2–B6.
- Rodríguez Tribaldos, V., White, N. J., Roberts, G. G., and Hoggard, M. J. (2017). Spatial and temporal uplift history of South America from calibrated drainage analysis. *Geochemistry, Geophysics, Geosystems*, 18(6):2321–2353.
- Savage, J. C., Svarc, J. L., and Yu, S.-B. (2005). Postseismic relaxation and transient creep. *Journal of Geophysical Research*, 110(B11):B11402.
- Saylor, J. E. and Horton, B. K. (2014). Nonuniform surface uplift of the Andean plateau revealed by deuterium isotopes in Miocene volcanic glass from southern Peru. *Earth and Planetary Science Letters*, 387:120–131.
- Schoenbohm, L. M. and Strecker, M. R. (2009). Normal faulting along the southern margin of the Puna Plateau, northwest Argentina. *Tectonics*, 28(5).
- Scholz, C. H. (1998). Earthquakes and friction laws. *Nature*, 391(6662):37–42.
- Scholz, C. H. (2002). *The Mechanics of Earthquakes and Faulting*. Cambridge University Press.
- Schurr, B., Asch, G., Rietbrock, A., Kind, R., Pardo, M., Heit, B., and Monfret, T. (1999). Seismicity and average velocities beneath the Argentine Puna Plateau. *Geophysical Research Letters*, 26(19):3025–3028.

- Scott, C., Lohman, R., Pritchard, M., Alvarado, P., and Sánchez, G. (2014). Andean earthquakes triggered by the 2010 Maule, Chile (Mw8.8) earthquake: Comparisons of geodetic, seismic and geologic constraints. *Journal of South American Earth Sciences*, 50:27–39.
- Sébrier, M., Mercier, J. L., Macharé, J., Bonnot, D., Cabrera, J., and Blanc, J. L. (1988). The state of stress in an overriding plate situated above a flat slab: The Andes of central Peru. *Tectonics*, 7(4):895–928.
- Sébrier, M., Mercier, J. L., Mégard, F., Laubacher, G., and Carey-Gailhardis, E. (1985). Quaternary normal and reverse faulting and the state of stress in the central Andes of south Peru. *Tectonics*, 4(7):739–780.
- Shako, R., Forste, C., Abrikosov, O., Bruinsma, S., Marty, J.-C., Lemoine, J.-M., Flechtner, F., Neumayer, H., and Dahle, C. (2014). EIGEN-6C: A High-Resolution Global Gravity Combination Model Including GOCE Data. *Observation of the System Earth from Space - CHAMP, GRACE, GOCE and future missions*, pages 155–161.
- Sibson, R. H. (2004). Controls on maximum fluid overpressure defining conditions for mesozonal mineralisation. *Journal of Structural Geology*, 26(6-7):1127–1136.
- Sladen, A., Tavera, H., Simons, M., Avouac, J. P., Konca, A. O., Perfettini, H., Audin, L., Fielding, E. J., Ortega, F., and Cavagnoud, R. (2010). Source model of the 2007 Mw 8.0 Pisco, Peru earthquake: Implications for seismogenic behavior of subduction megathrusts. *Journal of Geophysical Research*, 115(B2):B02405.
- Sloan, R. A., Jackson, J. A., McKenzie, D., and Priestley, K. (2011). Earthquake depth distributions in central Asia, and their relations with lithosphere thickness, shortening and extension. *Geophysical Journal International*, 185(1):1–29.
- Smith, J. A., Seltzer, G. O., Rodbell, D. T., and Klein, A. G. (2005). Regional synthesis of last glacial maximum snowlines in the tropical Andes, South America. *Quaternary International*, 138-139:145–167.
- Smith, S. W. and Wyss, M. (1968). Displacement on the San Andreas fault subsequent to the 1966 Parkfield earthquake. *Bulletin of the Seismological Society of America*, 58(6):1955–1973.
- Stewart, J. and Watts, A. B. (1997). Gravity anomalies and spatial variations of flexural rigidity at mountain ranges. *Journal of Geophysical Research: Solid Earth*, 102(B3):5327–5352.

- Suarez, G., Molnar, P., and Burchfiel, B. C. (1983). Seismicity, fault plane solutions, depth of faulting, and active tectonics of the Andes of Peru, Ecuador, and southern Colombia. *Journal of Geophysical Research*, 88(B12):10403–10428.
- Tavera, H. and Buforn, E. (2001). Source mechanism of earthquakes in Peru. *Journal of Seismology*, 5(4):519–539.
- Taymaz, T., Jackson, J., and Westaway, R. (1990). Earthquake mechanisms in the Hellenic Trench near Crete. *Geophysical Journal International*, 102(3):695–731.
- Thompson, S. C., Weldon, R. J., Rubin, C. M., Abdrakhmatov, K., Molnar, P., and Berger, G. W. (2002). Late Quaternary slip rates across the central Tien Shan, Kyrgyzstan, central Asia. *Journal of Geophysical Research: Solid Earth*, 107(B9):ETG 7–1–ETG 7–32.
- Tibaldi, A. and Bonali, L. I. (2018). Contemporary recent extension and compression in the central Andes. *Journal of Structural Geology*, 107:73–92.
- Tibaldi, A., Corazzato, C., and Rovida, A. (2009). Miocene-Quaternary structural evolution of the Uyuni-Atacama region, Andes of Chile and Bolivia. *Tectonophysics*, 471(1-2):114–135.
- Turcotte, D. L. and Schubert, G. (2002). *Geodynamics*. Cambridge University Press.
- Vega, A. and Buforn, E. (1991). Focal mechanisms of intraplate earthquakes in South America. *Pure and Applied Geophysics*, 136(4).
- Veloza, G., Styron, R., and Taylor, M. (2012). Open-source archive of active faults for northwest South America. *GSA Today*, 22(10):4–10.
- Villegas-Lanza, J. C., Chlieh, M., Cavalié, O., Tavera, H., Baby, P., Chire-Chira, J., and Nocquet, J. M. (2016). Active tectonics of Peru: Heterogeneous interseismic coupling along the Nazca megathrust, rigid motion of the Peruvian Sliver, and Subandean shortening accommodation. *Journal of Geophysical Research: Solid Earth*, 121(10):7371–7394.
- Ward, K. M., Zandt, G., Beck, S. L., Wagner, L. S., and Tavera, H. (2016). Lithospheric structure beneath the northern Central Andean Plateau from the joint inversion of ambient noise and earthquake-generated surface waves. *Journal of Geophysical Research: Solid Earth*, 121(11):8217–8238.
- Watts, A., Lamb, S., Fairhead, J., and Dewey, J. (1995). Lithospheric flexure and bending of the Central Andes. *Earth and Planetary Science Letters*, 134(1-2):9–21.

- Wdowinski, S., Oconnell, R. J., and England, P. (1989). A continuum model of continental deformation above subduction zones - Application to the Andes and the Aegean. *Journal of Geophysical Research-Solid Earth and Planets*, 94(B8):10331–10346.
- Weber, M. B. I., Tarney, J., Kempton, P. D., and Kent, R. W. (2002). Crustal make-up of the northern Andes : evidence based on deep crustal xenolith suites, Mercaderes, SW Colombia. *Tectonophysics*, 345:49–82.
- Weiss, J. R., Brooks, B. A., Foster, J. H., Bevis, M., Echalar, A., Caccamise, D., Heck, J., Kendrick, E., Ahlgren, K., Raleigh, D., Smalley, R., and Vergani, G. (2016). Isolating active orogenic wedge deformation in the southern Subandes of Bolivia. *Journal of Geophysical Research: Solid Earth*, 121(8):6192–6218.
- Wells, D. L. and Coppersmith, K. J. (1994). New empirical relationships among magnitude, rupture length, rupture width, rupture area, and surface displacement. *Bulletin of the Seismological Society of America*, 84(4):974–1002.
- Wessel, P., Smith, W. H. F., Scharroo, R., Luis, J., and Wobbe, F. (2013). Generic Mapping Tools: Improved Version Released. *Eos, Transactions American Geophysical Union*, 94(45):409–410.
- Whitman, D., Isacks, B. L., Chatelain, J.-L., Chiu, J.-M., and Perez, A. (1992). Attenuation of high-frequency seismic waves beneath the central Andean Plateau. *Journal of Geophysical Research*, 97(B13):19929.
- Zhou, R., Schoenbohm, L. M., and Cosca, M. (2013). Recent, slow normal and strike-slip faulting in the Pasto Ventura region of the southern Puna Plateau, NW Argentina. *Tectonics*, 32(1):19–33.
- Zwick, P., McCaffrey, R., and Abers, G. (1994). MT5 Program.

Tables

| Method | Strike | Dip | Rake | L , km | W , km | \bar{u} , m | M_0 , Nm |
|-----------------|-----------------|--------------|-----------------|----------|----------|------------------|----------------------------|
| gCMT | 148° | 43° | 274° | - | - | 0.4 [‡] | 2.2×10 ¹⁸ |
| USGS | 134° | 35° | 263° | - | - | 0.5 [‡] | 2.3×10 ¹⁸ |
| Ruptures | 130-145° | - | - | 12 | - | 0.1-0.3 | 0.4-1.3×10 ¹⁸ † |
| BWF | 144° (110-160°) | 39° (30-55°) | 276° (250-300°) | - | - | 0.2 [‡] | 0.8-1.4×10 ¹⁸ |
| InSAR | 135° (120-145°) | 40° (35-55°) | 250° (250-270°) | 13 | 12 | 0.5 | 2.4×10 ¹⁸ |

Table 1: Comparison of the source parameters determined from the surface ruptures, seismology and InSAR observations of the Parina earthquake. BWF indicates the long-period body-waveform solution. L and W are the along-strike length and down-dip width of the rupture patch, respectively. Moment is calculated using $M_0 = \mu A \bar{u}$, where μ is the shear modulus (30 GPa), A is the fault area and \bar{u} is the average fault slip. Values marked (†) have been calculated assuming the fault rupture is square (i.e. $L \approx W$), and values marked (‡) have been calculated assuming the fault is 13 km long and square. For the body-waveform and InSAR model the range of acceptable fault geometry parameters is given in brackets next to the best-fit value.













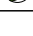
| Date | Time (GMT) | Lon, $^{\circ}$ | Lat, $^{\circ}$ | s/d/r | M_w | z, km | % DC | Mech |
|------------|------------|-----------------|-----------------|-------------|-------|-------|------|---|
| 1993 07 22 | 04:57:15 | -71.18 | 6.49 | 024/35/-93 | 6.4 | 18 | - |  , b |
| 1994 05 31 | 17:42:04 | -72.04 | 7.39 | 138/38/78 | 6.1 | 6 | - |  , b |
| 1995 01 19 | 15:05:11 | -72.94 | 5.04 | 214/57/97 | 6.5 | 21 | - |  , b |
| 1995 10 03 | 01:51:37 | -77.53 | -2.55 | 216/40/103 | 6.8 | 19 | - |  , b |
| 2001 06 29 | 22:30:21 | -70.35 | -15.37 | 110/58/-107 | 5.4 | 6 | 82 |  , a |
| 2001 08 12 | 00:16:32 | -70.03 | -16.76 | 130/45/-108 | 5.1 | 6 | 87 |  , a |
| 2006 08 09 | 22:36:11 | -70.75 | -14.45 | 082/51/-93 | 5.2 | 8 | 87 |  , a |
| 2009 11 06 | 08:50:02 | -64.46 | -23.44 | 224/30/131 | 5.4 | 20 | 92 |  , a |
| 2010 02 27 | 15:45:43 | -65.76 | -24.85 | 162/25/97 | 6.2 | 9 | 99 |  , B |
| 2011 10 06 | 11:12:37 | -64.22 | -24.18 | 176/56/91 | 5.9 | 15 | - |  , b |
| 2014 02 17 | 09:41:40 | -71.58 | 6.64 | 008/67/117 | 5.3 | 28 | 70 |  , a |
| 2015 11 29 | 18:52:59 | -64.65 | -23.56 | 222/29/129 | 5.8 | 4 | 98 |  , B |
| 2017 04 18 | 17:49:59 | -75.31 | -2.73 | 028/42/88 | 5.9 | 15 | 88 |  , B |

Table 2: Waveform modelling results for earthquakes in South America (not including Parina, see Table 1). % DC is the percentage double-couple of the gCMT moment tensor (as defined in Jackson et al. [2002]). Mechanisms with reference *a* are modelled by fitting vertical-component seismograms with synthetic waveforms following the methods of Maggi et al. [2000b] and Craig et al. [2012] based on Chapman [1978] and Kennett et al. [1995] (see Supplementary Information), whilst those with reference *b* are modelled using long-period body-waveform inversion. For events labelled *B* we fixed the earthquake mechanism and inverted for depth, source-time function and moment only.

| Test | | <i>Test 1: all</i> | | <i>Test 2: N. of Santa Cruz</i> | |
|------|----------|--------------------|------------|---------------------------------|------------|
| | | Megathrust | Topography | Megathrust | Topography |
| SV | RMS, deg | 29 | 9 | 42 | 7 |
| GPS | RMS, deg | 33 | 25 | 42 | 31 |

Table 3: Results of a statistical comparison between the azimuth of the GPS velocity field and slip vectors (SV) in the eastern Andes, with the elastic model of strain accumulation on the Peru-Chile megathrust from Bevis et al. [2001] and the azimuth of topographic gradients [e.g. Copley and McKenzie, 2007]. A map view of the measurement sites and their azimuths is shown in Fig. 9b. Topographic gradients were calculated from a 300 km Gaussian filtered version of the SRTM 3-arcsecond elevation model [Farr et al., 2007]. Filter widths between 100-400 km give similar results. RMS is the root-mean square misfit between the observed and modelled azimuth. Two tests are shown, one in which all GPS and slip vector measurements shown in Fig. 9b are used to compute the misfits (Test 1), and one in which only measurements from north of Santa Cruz are used to compute the misfits (Test 2). In all cases the azimuth of the topographic gradients fit the observations better than the model of elastic strain accumulation of Bevis et al. [2001].

| Variable | Value | Source |
|---|---|---|
| Crustal thickness, lowlands | 35-45 km | [Assumpção et al., 2013] |
| Crustal thickness, Andes | 65-80 km | [Assumpção et al., 2013] |
| Lithosphere thickness, lowlands | 120-140 km | [McKenzie and Priestley, 2008] |
| Lithosphere thickness, Andes | 180-220 km or 0 km | [see Supplementary Information] |
| Moho temperature, lowlands | 600-700 °C | [see Supplementary Information] |
| Moho temperature, Andes | 700-1000 °C | [Weber et al., 2002] |
| Mantle potential temperature | 1315 °C | [McKenzie et al., 2005] |
| Thermal expansivity [†] , crust | $3 \times 10^{-5} \text{ K}^{-1}$ | [Turcotte and Schubert, 2002] |
| Thermal expansivity [†] , mantle | $3 - 4.5 \times 10^{-5} \text{ K}^{-1}$ | [Bouhifd et al., 1996] |
| Asthenosphere density (ρ_a , 0 °C) | 3330 kg m ⁻³ | [Turcotte and Schubert, 2002] |
| Lithospheric Mantle density (0 °C) | $\rho_a - 50 \text{ kg m}^{-3}$ | [Lucassen et al., 2005; McKenzie and Priestley, 2016] |
| Crustal density (0 °C) | 2800 kg m ⁻³ | [Lucassen et al., 1999] |
| Foreland fault dips | 30-50° | [This study] |
| Activation energy (E) | 540 kJ mol ⁻¹ | [Karato and Wu, 1993] |
| Activation volume (V) | 20 cm ³ mol ⁻¹ | [Karato and Wu, 1993] |
| Stress exponent (n) | 3 | [Karato and Wu, 1993] |
| Seismogenic thickness | 40-45 km | [Assumpção and Suarez, 1988] |
| Foreland sediment thickness | 5-8 km | [McGroder et al., 2015] |
| Neutral fibre depth | 13-28 km | [see Section 3.5] |
| Elastic core thickness [‡] | 1-20 km | [see caption] |

Table 4: Parameters used in the calculations for the force exerted between the mountain range and forelands, and for estimating the frictional strength of faults in the South American forelands. (†) This is the linear coefficient of thermal expansion. (‡) The elastic core thickness is the extent of the region either side of the neutral fibre in the bending South American foreland over which the stress field changes from being extensional to compressional.

Figures

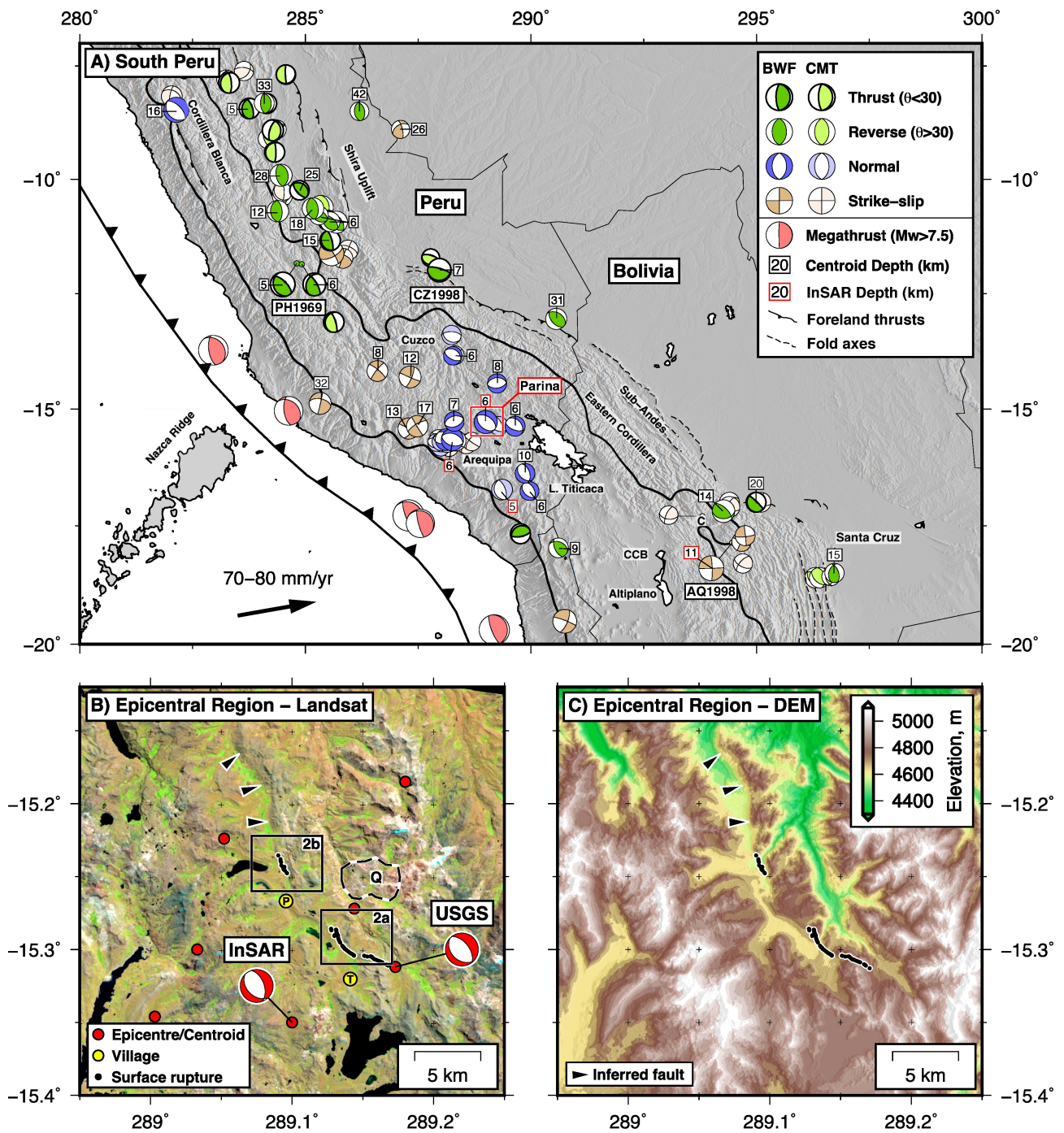


Figure 1: Overview of the Parina earthquake epicentral region. Waveform modelled (BWF) and global catalogue earthquakes (gCMT; Ekström et al. [2012]) with $M_w > 5$ in the overriding plate are shown in (a) (see Supplementary Table 1 for sources). We do not include earthquakes offshore in the forearc. PH1969 are the 1969 Pariahuanca earthquakes [Philip and Megard, 1977; Suarez et al., 1983], AQ1998 is the 1998 Aiquile earthquake [Funning et al., 2005] and CZ1998 is the 1998 Cuzco foreland earthquake [Emmerson, 2007]. C marks the Cochabamba and Punata basins, and CCB marks the Corque-Corococo Basin. The thick black line is the 3000 m contour from the 100 km Gaussian filtered topography. The red box marks the location of (b) and (c). (b) is a Landsat 8 (bands 4,3,2) image of the epicentral region. Black dots are the co-seismic surface ruptures, and black triangles mark the inferred extension of the Parina Fault north of the surface ruptures. P and T marks the villages of Parina and Togra. The centroid and mechanism of the best-fit InSAR fault plane, and the epicentre of the USGS source model, are shown together with the epicentres of $M_w > 4.0$ NEIC aftershocks (location error > 5 km). Black boxes outline the locations of the satellite imagery in Figure 2, and the region marked ‘Q’ is an open cast quarry. (c) is the SRTM 1-arcsecond topography covering the same region as (b), highlighting the NW-SE trending step in topography associated with the Parina Fault.

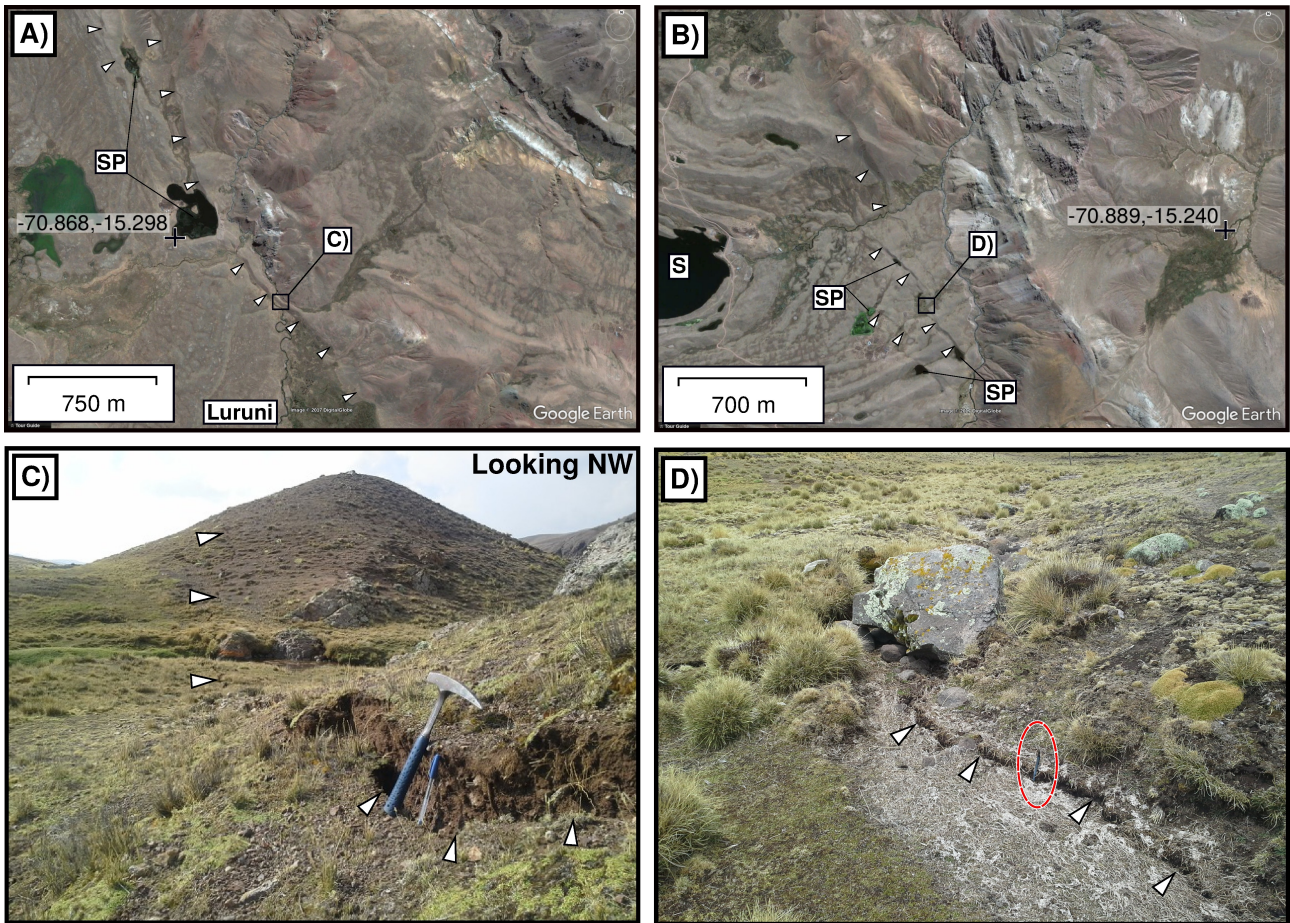


Figure 2: Geomorphology and surface ruptures of the 1st December 2016 Parina earthquake. (a) shows a GoogleEarth satellite image (from 2015) of the southern end of the co-seismic ruptures near Togra (see Fig. 1b). White triangles pick out small scarps in the topography that are associated with the mapped co-seismic surface ruptures, and bodies of water marked SP are small ponds dammed against the footwall scarp of the Parina Fault. (b) shows a similar GoogleEarth image (from 2015) over the northern end of the ruptures near Saguanani Lake (marked S). The vertical offsets across the surface ruptures in the southern section are up to 30 cm in height (c, geological hammer for scale) and have a small opening component, whilst at the northern end of the rupture, most of the features are hairline ruptures and have <10 cm offset (d, pen circled in red for scale).

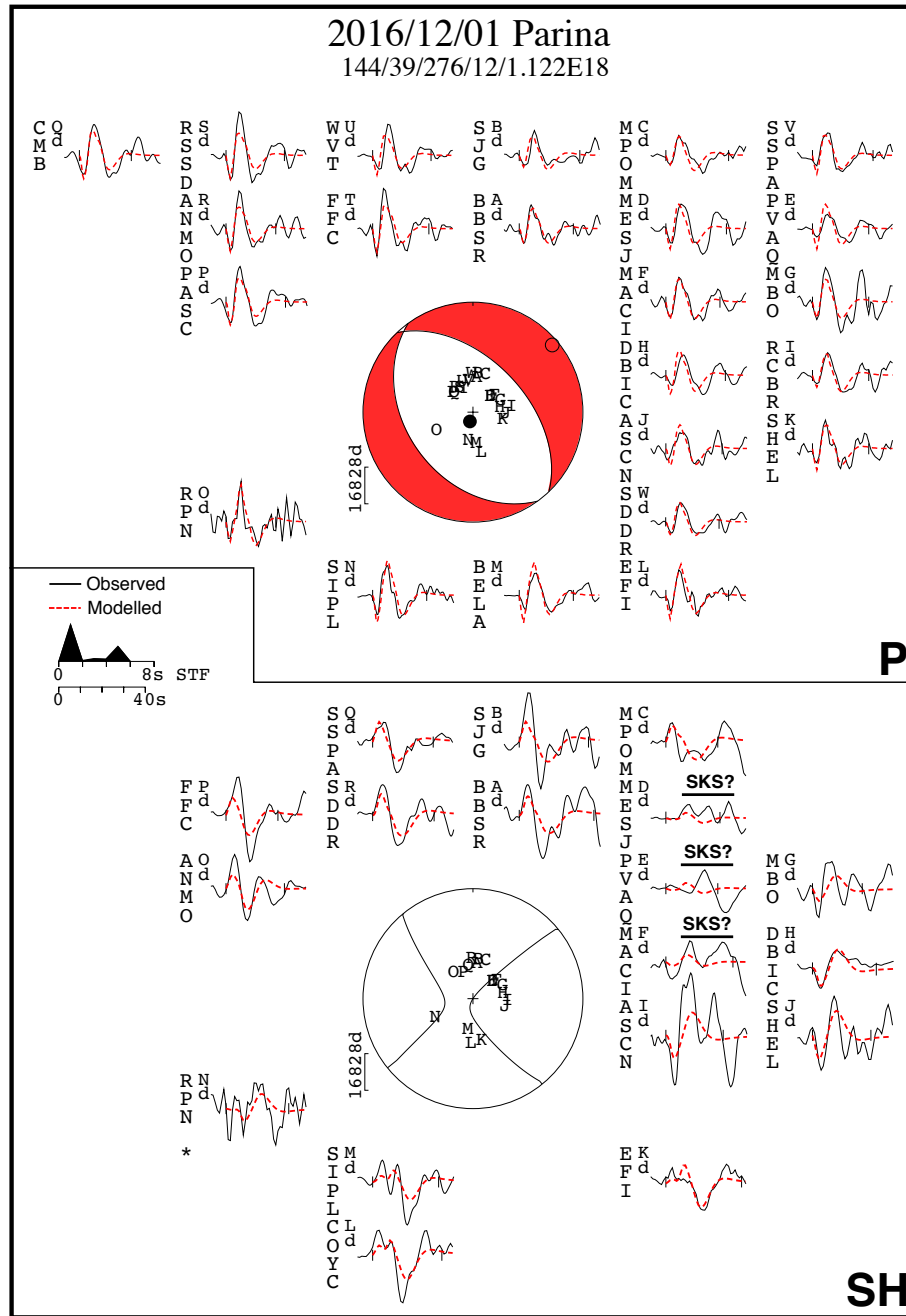


Figure 3: Minimum-misfit teleseismic body-waveform solution for the 1st December 2016 Parina earthquake. Details of the inversion result are shown below the title with the form strike/dip/rake/depth/moment, where depth is in kilometres and moment is in Nm. The top panel shows a lower hemisphere projection of the P wave nodal planes, with the station distribution used in the best-fit inversion shown as capital letters. Observed and modelled seismograms are 40 second time-series and are shown as black and red dashed lines, respectively. The seismogram station code is shown to the left of the corresponding seismogram, and the inversion time window is demarcated by vertical black ticks. P and T axes are projected onto the focal sphere as a black filled circle and an open circle, respectively. The lower panel shows the equivalent for the SH waves. Seismograms that are labelled with SKS occur within the $80\text{--}85^\circ$ range from the epicentre, therefore may contain some signal from phases that have interacted with the core. Stations with an asterisk are weighted to 0 in the inversion as they contain a large component of noise, but are included for comparison with the model predictions. The source-time function is shown as black triangles.

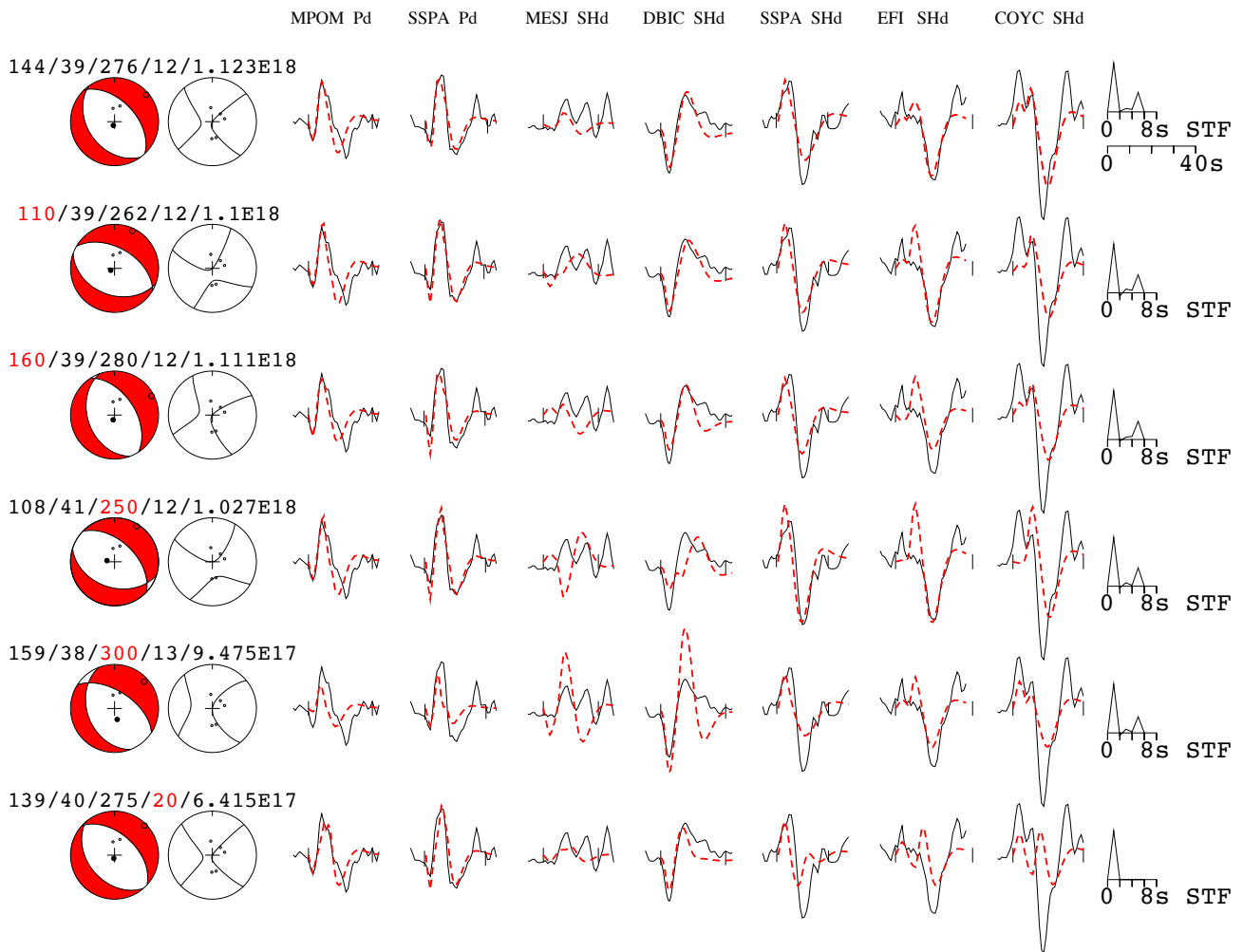


Figure 4: Sensitivity tests showing fits between selected waveforms of the 2016 Parina earthquake given variations in the source parameters. Each line shows *P* and *SH* focal spheres, the fault parameters in strike/dip/rake/centroid depth/moment formation, the fit between modelled (red dashed) and observed (black solid) waveforms at a set of stations, and the source-time function for that particular model. The station codes are given at the top in each column, where Pd are vertical-component waveforms and SHd are transverse waveforms. The best-fit model presented in Fig. 3 is shown on the top row, and each subsequent row shows different inversion results in which the parameter in red is held fixed, whilst all other parameters can vary.

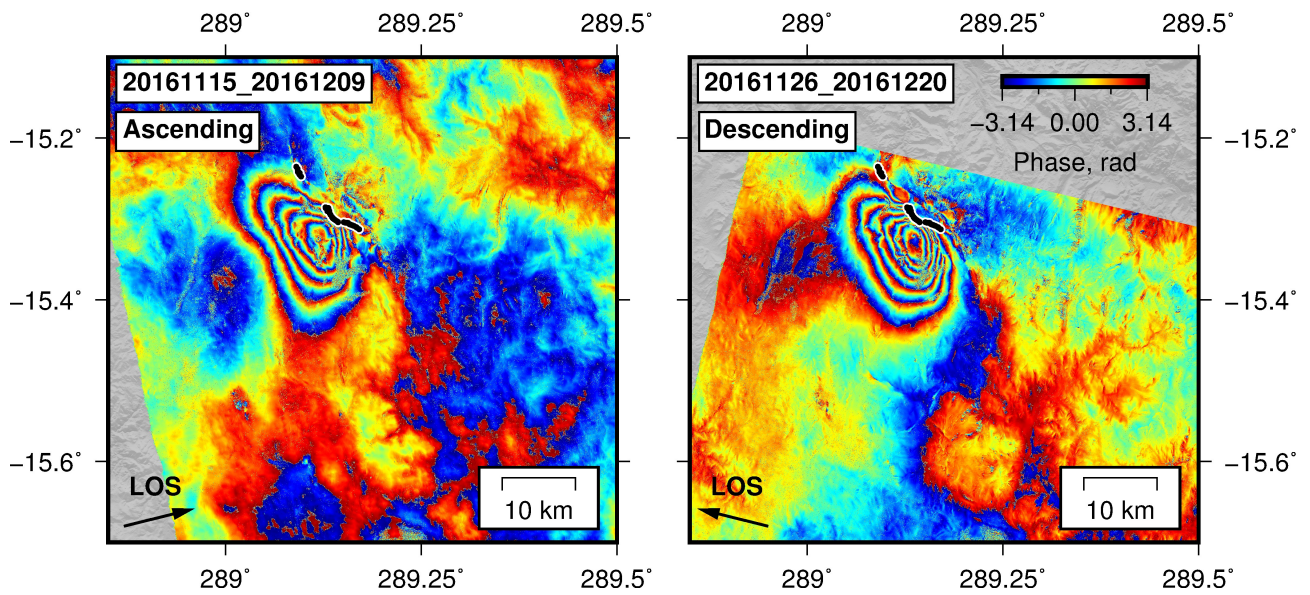


Figure 5: Wrapped co-seismic interferograms covering the 1st December 2016 Parina earthquake. The dates of the pre- and post-event acquisitions are given in the form YYYYMMDD, and the line-of-sight vector is shown in the bottom left. The incidence angle of this vector relative to the Earth's surface is between $30\text{-}43^\circ$. Black dots outline the locations of the co-seismic surface ruptures.

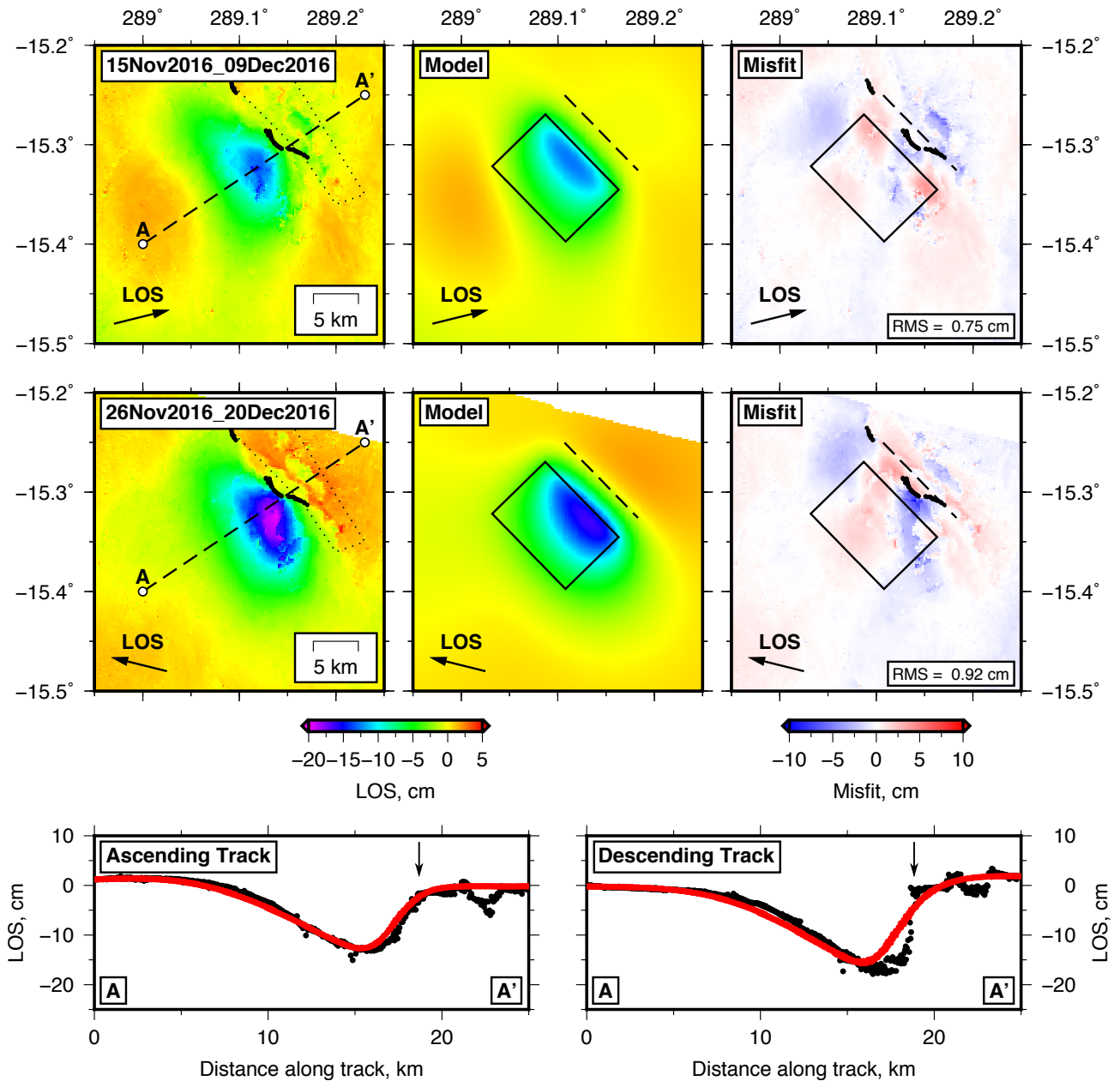


Figure 6: Results of inversions for the best-fitting elastic dislocation model to the observed InSAR surface displacements. The left panels show the unwrapped and downsampled interferograms covering the co-seismic period. We use the convention that +ve LOS is motion towards the satellite. The black polygon delineates a region with short wavelength, spatially variable LOS displacements that are likely to represent offsets at the surface generated by local slope failure in the steep valley NE of Parina, and open cast quarrying activity (Fig. 1b). The black dots are the mapped co-seismic surface ruptures. The best-fitting model is shown in the middle panels, with the map view of the fault plane shown as a black rectangle, and its surface projection as a black dashed line. The misfit between the observations and models is shown in the panels on the right. Profiles between A-A' through the observations (black dots) and models (red dots) are shown below. Steep gradients of LOS displacement near the surface ruptures (shown by the vertical arrows) are clear in the descending-track profile, however are not present in the smoother ascending track data. These differences between the surface displacement may reflect post-seismic afterslip, as the descending track acquisition was collected 19 days after the earthquake, whilst the ascending track data only includes 8 days of post-seismic deformation. We present models and a discussion of the post-seismic deformation in Section 2.5.

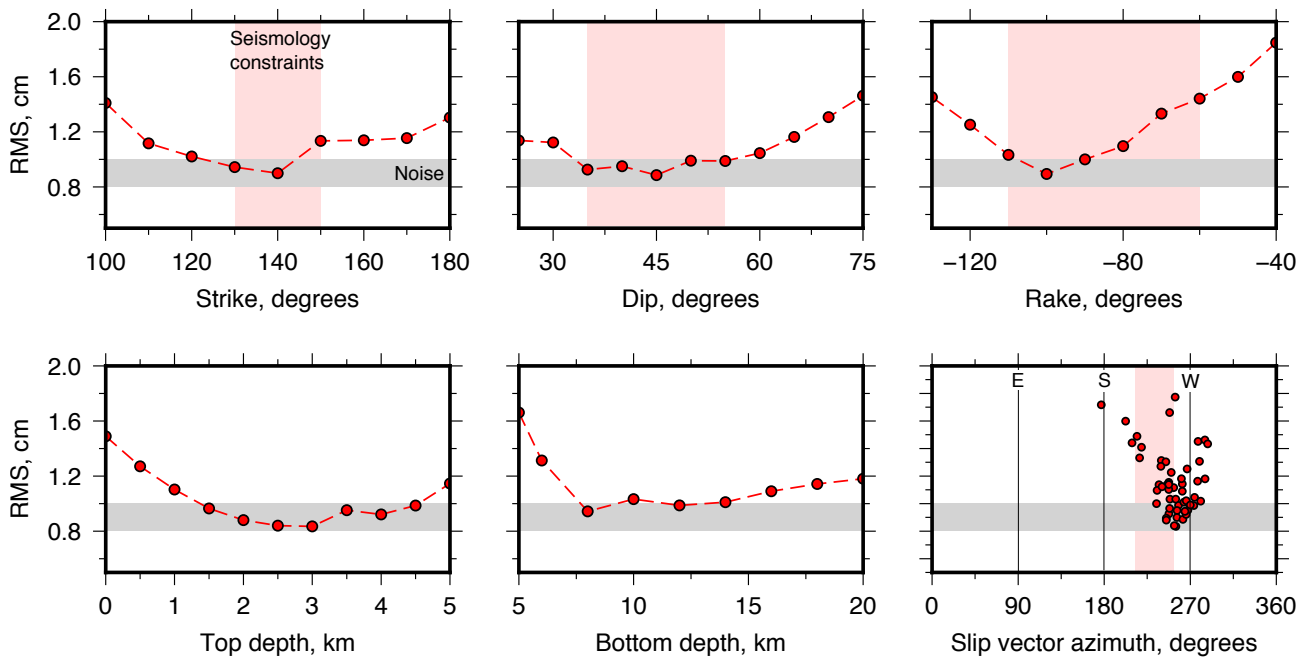


Figure 7: Sensitivity analysis of the InSAR inversions to the fault parameters. The light red bars mark the possible range of fault parameters determined from the seismological body-waveform modelling (Figs. 3,4) and the orientation of the surface ruptures. The grey bar shows the noise levels in the interferograms. The slip vector azimuth is given as the motion of the footwall relative to the hangingwall in degrees clockwise from north.

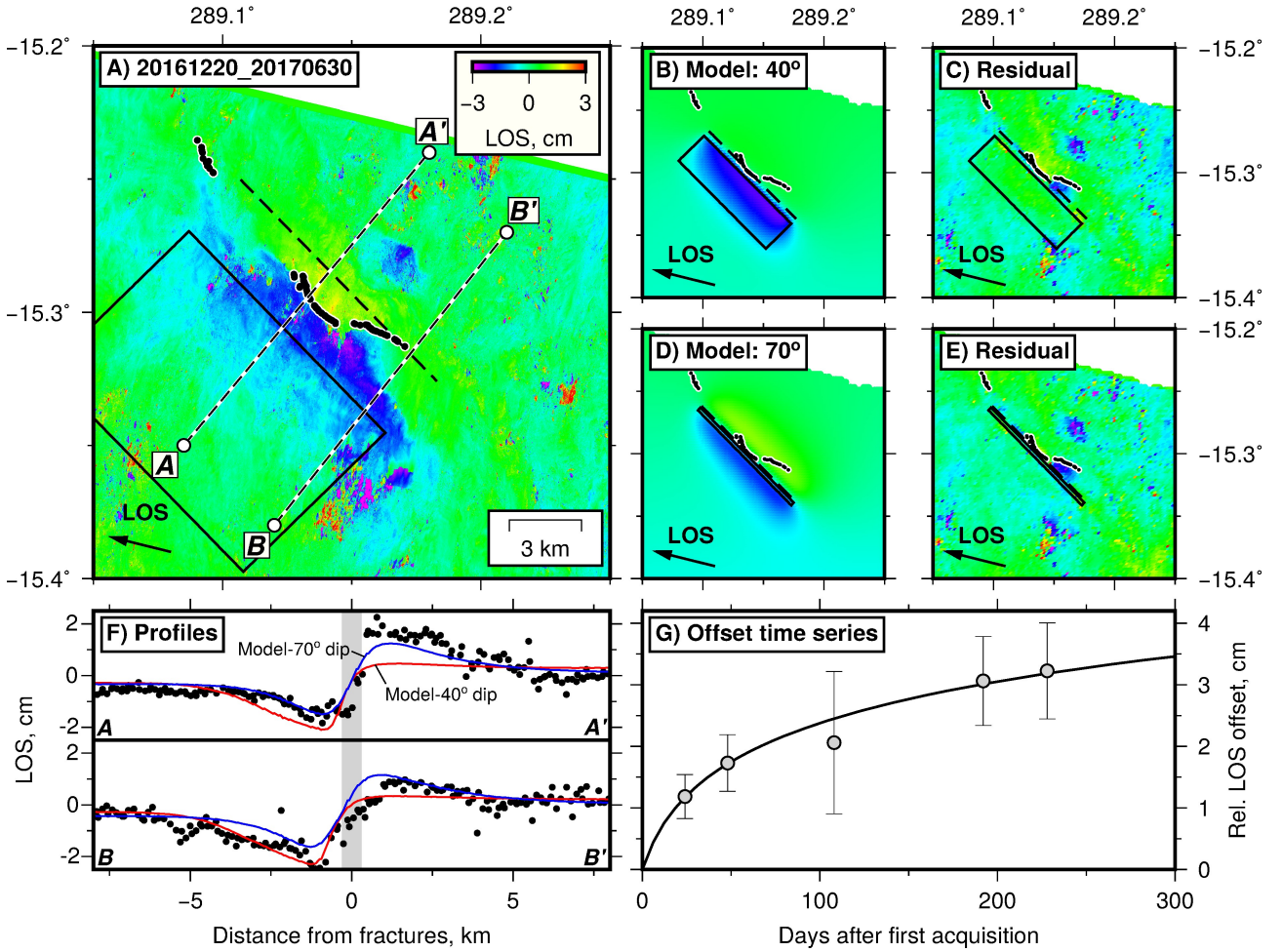


Figure 8: Post-seismic deformation following the 2016 Parina earthquake. (a) shows a descending-track interferogram covering 6 months of post-seismic deformation with a linear, long-wavelength ramp removed. The pre- and post-event acquisition dates are given in YYYYMMDD format in the top left, and the black dots are the co-seismic surface ruptures. The map view of the best-fit co-seismic fault plane is shown as a black solid line, and its surface projection as a black dashed line. (b) shows the best-fit fault model to the post-seismic surface displacement when the fault strike, dip and rake are fixed to the co-seismic fault plane. (c) shows the residual between the model prediction and the observed surface displacement. (d) and (e) show the best-fit fault model when the strike and rake are fixed to their co-seismic values, and the dip is fixed to 70° . Profiles through the deformation field between A-A' and B-B' are shown in (f), where the black dots are the observed LOS changes, the red lines are the model in (b), the blue lines are the model in (d), and the grey bar denotes the location of the surface ruptures. The temporal evolution of deformation in (g) records the change in relative LOS between the immediate hangingwall and footwall of the Parina Fault derived from a series of interferograms with a common reference. Error bars are the 1 standard deviation bounds on the difference in LOS offset between the immediate hangingwall and footwall of the fault. The black solid line is a best-fit curve of the form $a \ln(1 + t/t_r)$, showing that the post-seismic deformation decays with the logarithm of elapsed time [e.g. Smith and Wyss, 1968; Savage et al., 2005; Fielding et al., 2009].

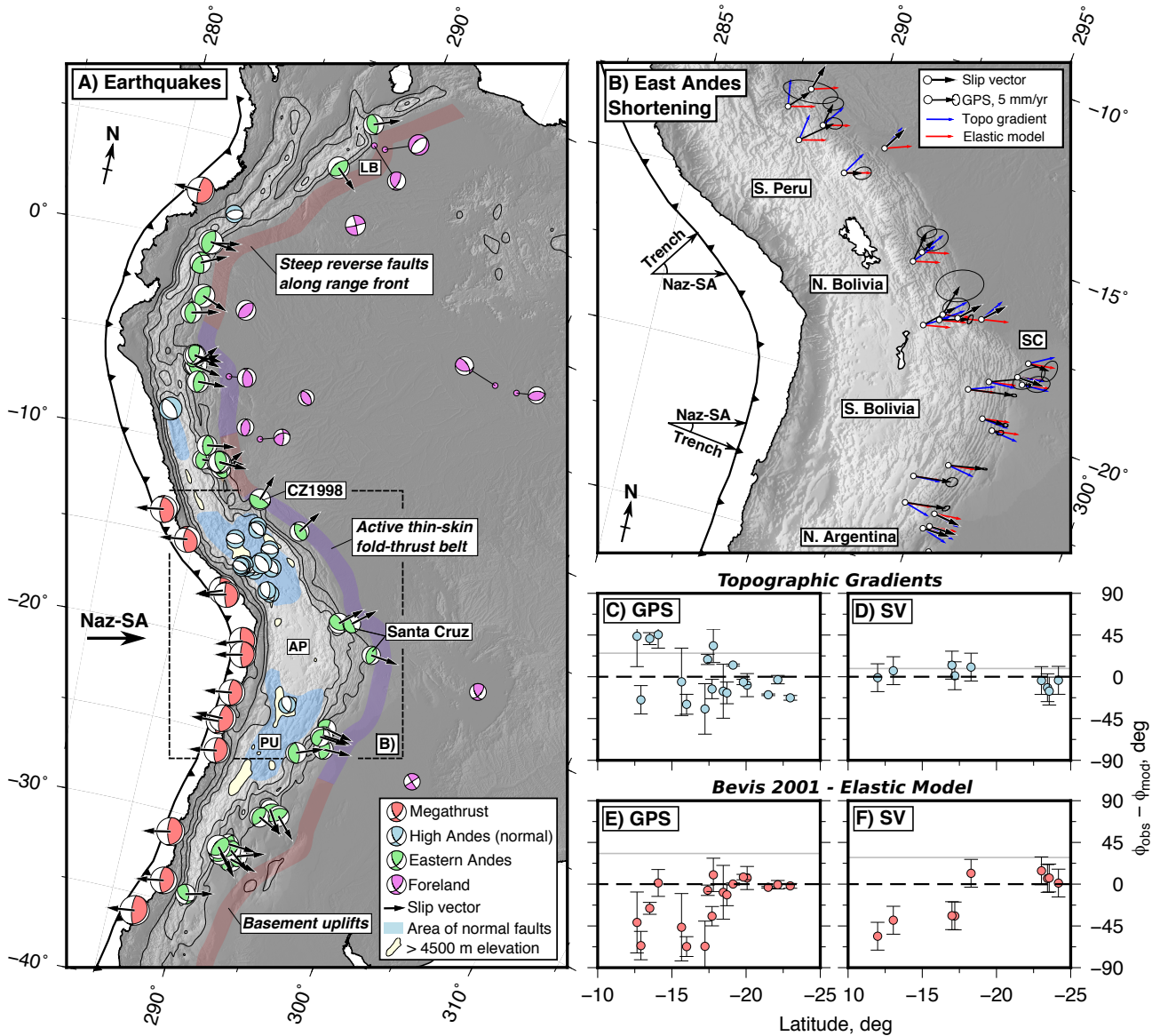


Figure 9: Earthquake and GPS data demonstrating the pattern of deformation in the regions bounding the Andes. (a) shows selected waveform-modelled earthquakes and well-constrained gCMT events compiled from the literature and this study (see Supplementary Table 1 and 2 for a list of sources). Thin lines are the 1, 2, 3 and 4.5 km elevation contours from the Gaussian filtered topography (300 km filter width). The light blue region is the area in which evidence for recent extension has been documented in the high Andes (Supp. Fig. 17). LB is the Llanos Basin, AP is the Altiplano, PU is the Puna plateau and SC is Santa Cruz. Both (a) and (b) are in oblique Mercator projection about the Euler pole of the Nazca-South America convergence taken from DeMets et al. [2010], therefore slip vectors parallel to relative plate motion will be horizontal [McKenzie and Parker, 1967]. (b) shows the azimuth of shortening in the eastern Andes inferred from selected GPS sites [Kendrick et al., 2001; Weiss et al., 2016] and earthquake slip vectors, compared with gradients in the filtered topography (300 km Gaussian filter) and the elastic block model of Bevis et al. [2001]. GPS velocities in (b) are shown relative to stable South America with 1σ uncertainty ellipses. (c-d) compare the azimuth of the topographic gradients with the azimuth of the GPS and earthquake slip vectors, respectively. (e-f) compare the predicted azimuths for the block model of Bevis et al. [2001] with the GPS and earthquake slip vectors. The grey lines show the the root-mean square misfit (always positive), see also Table 3.

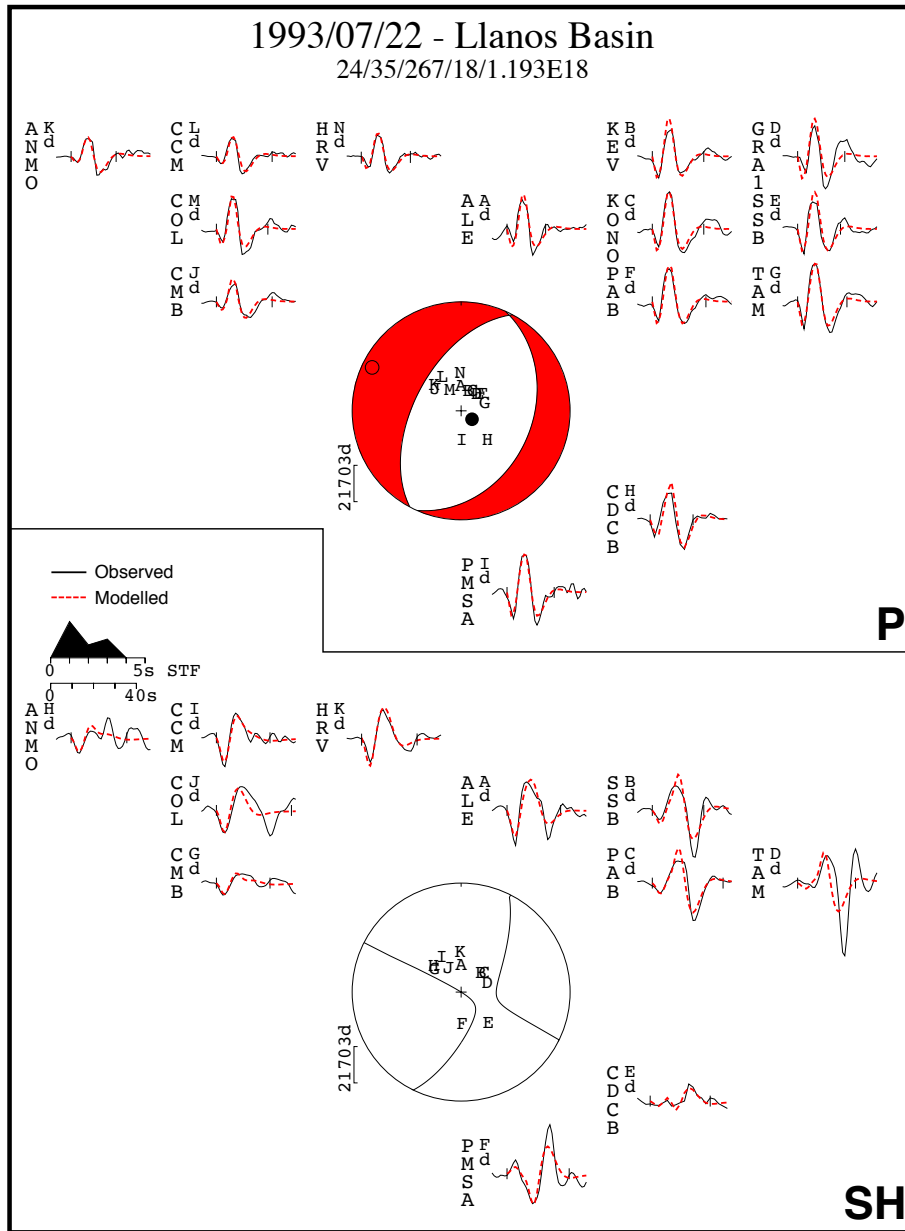


Figure 10: Minimum-misfit teleseismic body-waveform solution for the 22nd July 1993 Llanos Basin earthquake. Figure layout is the same as for Fig. 3. The uncertainties in the fault parameters were estimated using the method described in Section 2.2 and are strike = $\pm 25^\circ$, dip = $\pm 5^\circ$, rake = $\pm 25^\circ$ and depth ± 5 km.

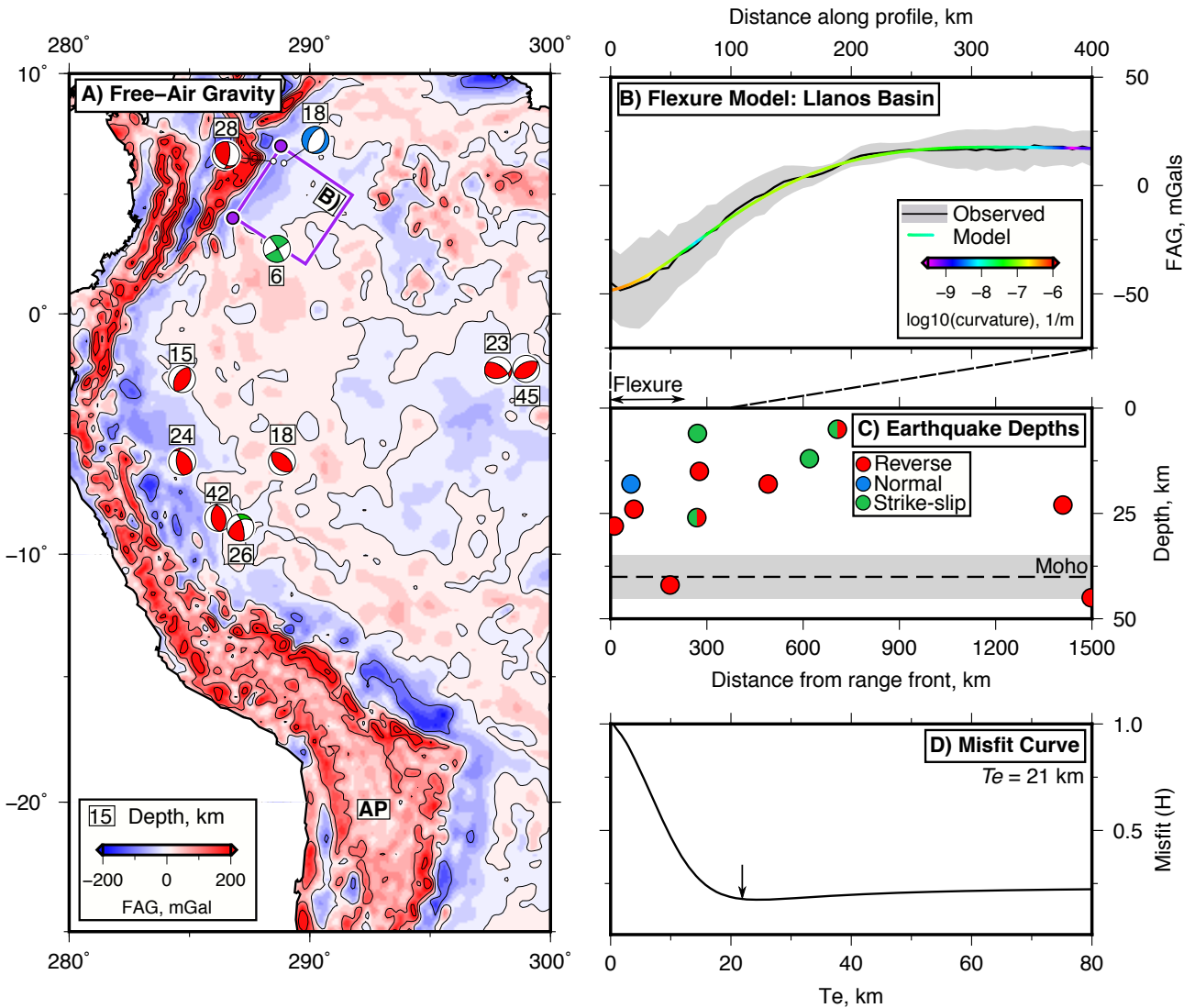


Figure 11: Free-air gravity data, earthquakes and plate models used to study the flexure of the South American forelands. (a) shows the EIGEN-6c free-air gravity map of South America [Shako et al., 2014] low-pass filtered to exclude signals with wavelength < 50 km that are unrelated to flexure [e.g. Bry and White, 2007]. The purple box is the region within which profiles through the gravity field perpendicular to the Andes range front have been extracted and stacked. AP marks the Altiplano. (b) shows the stacked free-air gravity anomalies with 1 standard deviation (σ) bounds, and the best-fit model to the observed gravity profile of an elastic plate overlying an inviscid half-space bending in response to a line load and bending moment [e.g. Turcotte and Schubert, 2002]. We assume that the sediments in the foreland basin are 500 kg m^{-3} less dense than the mantle beneath the plate, and Young's modulus and Poisson's ratio of the plate are 10^{11} Pa and 0.25, respectively [Turcotte and Schubert, 2002]. The colour of the line shows the absolute curvature of the plate model. (c) shows the mechanisms of waveform-modelled foreland earthquakes as a function of distance from the Andes range front. The Moho depth and uncertainty (1σ) is taken from the catalogue of Assumpção et al. [2013]. (d) is the weighted misfit between the model and observations computed for a range of elastic thicknesses, defined as $H = \frac{1}{N} \sum \left[\frac{g_m - g_o}{\sigma} \right]^2$, where g_m and g_o are the modelled and observed free-air gravity, respectively, and N is the number of measurements along the profile.

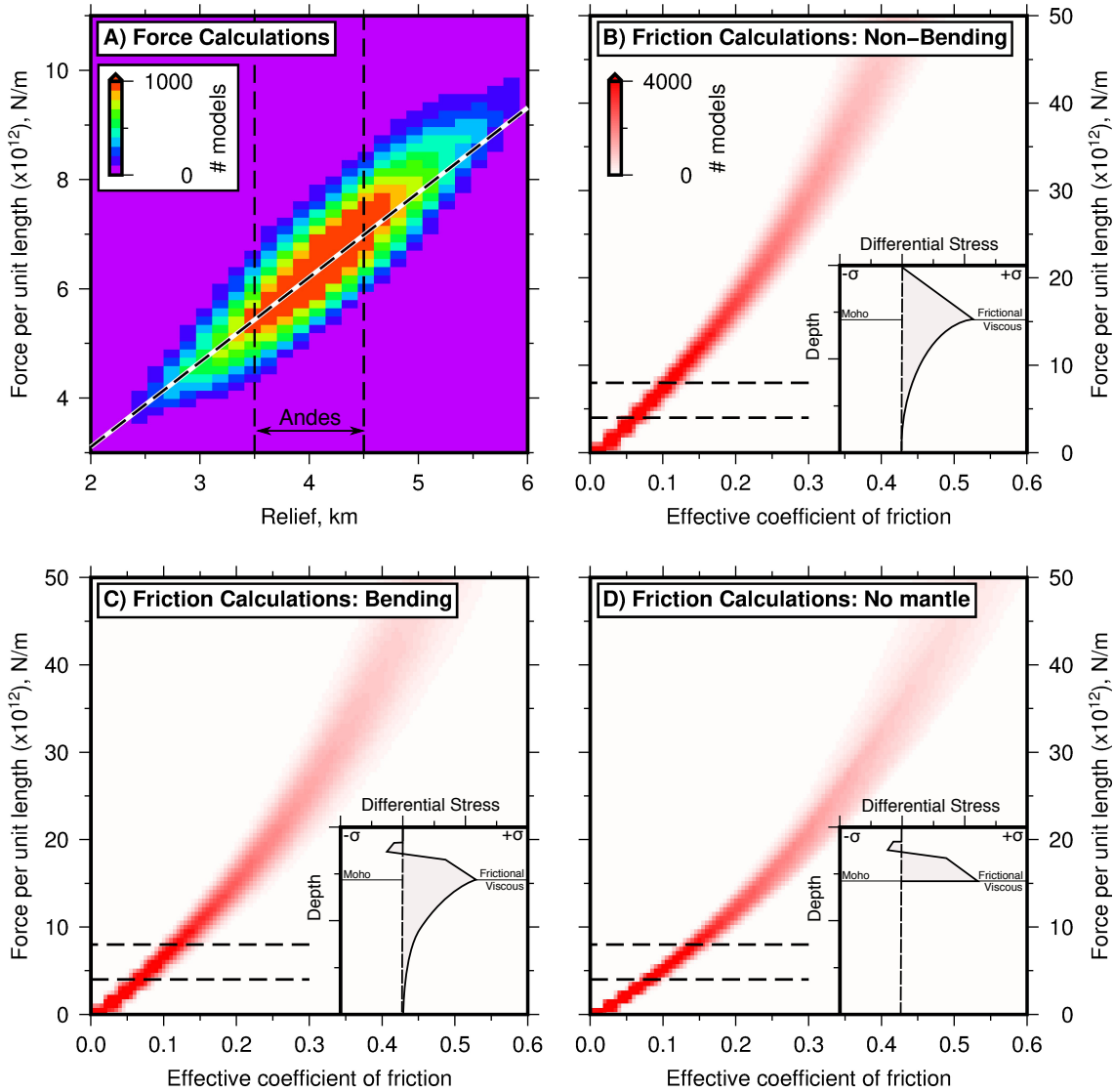


Figure 12: Results of calculations for the forces per unit length acting through the South American lithosphere, due to differences in gravitational potential energy between the Andes and the South American forelands. (a) shows the force calculations as a function of relief between the mountains and forelands (described in Section 4.1). Vertical black dashed lines delineate the range of appropriate solutions for the Andes. The dashed black and white line defines the relationship between relief and force assuming crustal isostasy, with a crustal thickness of 70 km and 40 km in the mountains and lowlands, respectively. (b,c,d) show the results of calculations for the maximum force that can be supported by the foreland lithosphere as a function of the effective coefficient of friction along faults, as described in the Section 4.2. The three different cases shown are; (b) when the whole crust is in compression and there is no sediment layer (i.e. the foreland outside the bending region); (c) when the top 5–8 km of crust is sediment that supports no force, the top 5–13 km of basement is in extension, and the bottom ~ 20 km is in compression (i.e. the foreland in the bending region); and (d) the end-member scenario when the lithosphere is bending, and the mantle supports no stress at all. Schematic yield stress profiles are shown inset. Horizontal black dashed lines are the bounds on the horizontal force acting through the South American lithosphere from the calculations in (a). Where the envelope of models plots above these horizontal dashed lines, the lithosphere would be too strong to break in earthquakes in response to the forces generated by contrasts in gravitational potential energy acting between the mountains and forelands.

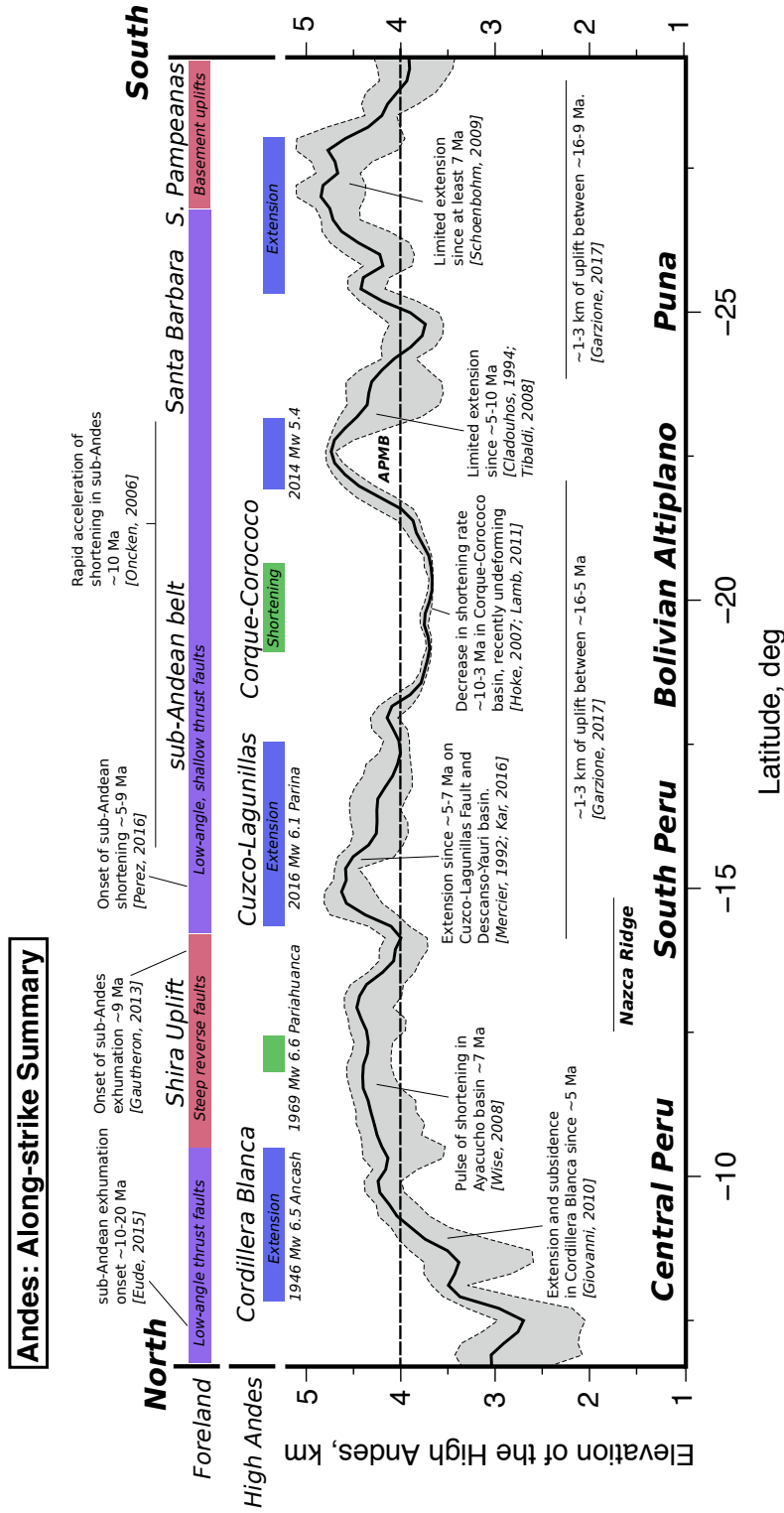


Figure 13: Summary of the topography and recent deformation history in the Andes between central Peru and northern Argentina. Topography is extracted in a 30 km swath down the spine of the range from a 100 km Gaussian filtered version of the SRTM 3-arcsecond elevation model. The maximum, mean and minimum elevations are shown. Evidence for the timing and pattern of deformation in the high Andes and the adjacent foreland is summarised above and below the elevation curve. APMB is the Altiplano-Puna magma body.

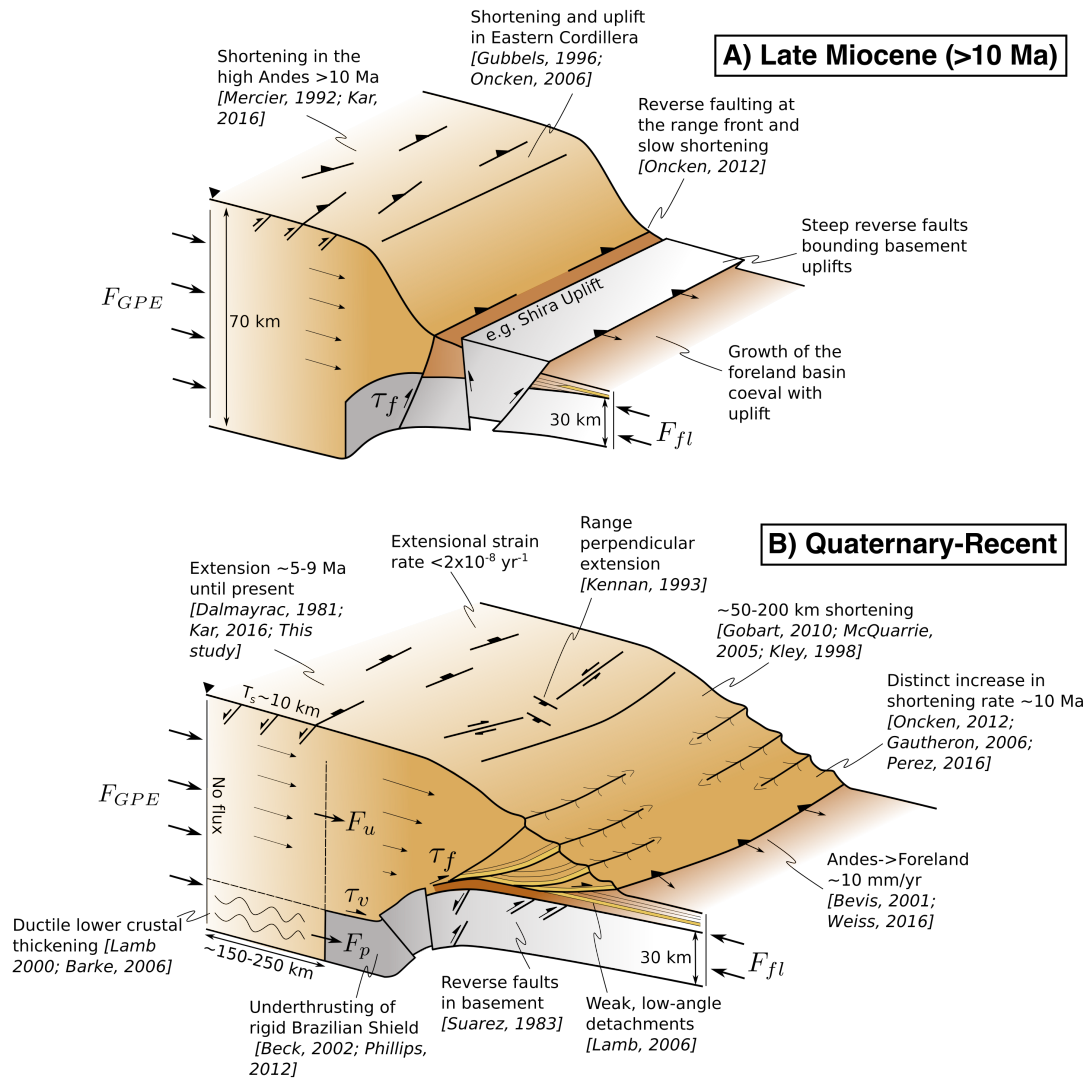


Figure 14: Sketch of the evolution of faulting in the Andes since the late Miocene. A reduction in the frictional shear stresses (τ_f) along the base of the eastern Andes ~5-9 Ma would have reduced the horizontal force acting through upper crust overriding the rigid foreland (F_u). A reduction in τ_f would be balanced ($F_{GPE} = F_u + F_p$) by an increase in the viscous resistance to shortening in the ductile lower crust (F_p), extensional viscous strain within the centre of the mountain belt, and an increase in the rate of propagation of the mountains over the rigid foreland.